Accepted Manuscript

Two billion years of evolution enclosed in hydrothermal rutile: Recycling of the São Francisco Craton Crust and constraints on gold remobilisation processes

Inês Pereira, Craig Storey, James Darling, Cristiano Lana, Ana R. Alkmim

PII: S1342-937X(18)30305-8
DOI: https://doi.org/10.1016/j.gr.2018.11.008
Reference: GR 2063

To appear in: *Gondwana Research*

Received date: 16 May 2018
Revised date: 25 October 2018
Accepted date: 1 November 2018

Please cite this article as: Inês Pereira, Craig Storey, James Darling, Cristiano Lana, Ana R. Alkmim , Two billion years of evolution enclosed in hydrothermal rutile: Recycling of the São Francisco Craton Crust and constraints on gold remobilisation processes. Gr (2018), https://doi.org/10.1016/j.gr.2018.11.008

TWO BILLION YEARS OF EVOLUTION ENCLOSED IN HYDROTHERMAL RUTILE: RECYCLING OF THE SÃO FRANCISCO CRATON CRUST AND CONSTRAINTS ON GOLD REMOBILISATION PROCESSES

Inês Pereira[1]

Craig Storey[1]

James Darling[1]

Cristiano Lana[2]

Ana R. Alkmim[2]

[1]School of Earth and Environmental Sciences, University of Portsmouth, Portsmouth, PO1 3QL, Hampshire, United Kingdom

[2]Applied Isotope Research Group, Departamento de Geologia, Universidade Federal de Ouro Preto, Ouro Preto, MG 35400000, Brazil

Corresponding author: ines.pereira@port.ac.uk

ABSTRACT

The Quadrilátero Ferrífero in the São Francisco Craton, Brazil is known for its world-class gold deposits hosted by the Rio das Velhas greenstone belt (RdV). As in other greenstone belts, gold is also concentrated in late Archean/early Paleoproterozoic supracrustal units; in this case within the Moeda Formation. This unit has been compared to the Witwatersrand basin where there has been a long-term debate over the nature of the gold and whether it is detrital (placer), hydrothermal or hybrid (modified placer). Presently, links between gold in the Moeda Formation and RdV are tenuous. To enlighten this area of ambiguity, a new approach using chemical, isotopic and mineral inclusion data from detrital rutile found in the gold-bearing horizons of the Moeda Formation is presented. Grain textures and mineral inclusions have contributed to establishing a primary hydrothermal origin for the rutile, related to As-Fe-Cu-Sb-Pb-W rich mineralising fluids. Fe, Nb and V indicate that the likely source of the gold-related rutiles is the Archean banded iron formations within the RdV, where most of the lode-gold occurs. Average Nb/Ta values of these rutiles are lower than average continental crust ratios which suggests fractionation driven by fluid precipitation and/or competing mineral phases. U-Pb data yield primary crystallisation ages older than deposition ages (> 2.58 Ga), supporting the detrital nature of these rutiles. Rutiles record

either resetting or new growth at 2.1 Ga and at ca. 500 Ma, during which gold was remobilised. Hence, this study supports a modified placer model for the gold-bearing horizons of the Moeda Formation. These fluid-assisted gold remobilisation events can be found in other correlated Paleoproterozoic gold-bearing horizon units that represent intracratonic basins related to the rifting of the Kenorland Supercontinent. This study reinforces the suitability of rutile and mineral inclusions as a powerful tool to elucidate processes and provenance.

Keywords: São Francisco Craton; paleoplacer; rutile; mineral inclusion; gold remobilisation

1. INTRODUCTION

Gold has recurrently been mobilised and concentrated in the Earth's crust over billions of years through multiple processes. These have led to the existence of many different types of gold deposits. Orogenic lode-gold is one of the most prominent types, both in terms of global distribution and gold endowment, and are genetically linked to convergent tectonics and/or supercontinent formation (Goldfarb et al., 2001; Lipson, 2014). These deposits have also been a main source for many paleoplacer districts throughout continents and across time (*e.g.* Witwatersrand, South Africa; Jacobina, Brazil; Huronian, Canada; Sierra Nevada, USA). In 2013, approximately 30% of global gold production (about 52 000 metric tons) was mined from placer districts worldwide (Frimmel, 2014; Lipson, 2014). Placer gold has historically been envisaged as an indicator of significant ore deposits in the basement source (*e.g.* Chapman et al., 2000), with remarkably high gold grades found (average of 11 g/t Au in the Witwatersrand deposit; Frimmel, 2014). Understanding paleoplacer formation has refined models used in exploration geology, and the sediments offer tremendously versatile detrital records of basement evolution, including evolution of magmatism, metamorphism, tectonism, and atmospheric redox conditions (*e.g.* Rasmussen and Buick, 1999; Frimmel, 2005; Goto et al., 2013; Ono and Fayek, 2011*;* Mukhopadhyay et al., 2016).

By far the most productive of the paleoplacer districts is the Witwatersrand deposit, with more than 50,000 metric tons of mined gold (Frimmel, 2014), formed as a Mesoarchean basin in the Kaapvaal craton. Many different models for the origin of the gold have been

proposed to account for the textural, mineralogical, and isotopic characteristics of the Au-bearing conglomerates of the Witwatersrand deposit, including detrital (*e.g.* Kirk et al., 2001), modified placer (*e.g.* Mathur et al., 2013) and hydrothermal (*e.g.* Phillips and Powell, 2015). Gold is highly susceptible to remobilisation and recrystallization during weathering due to its soft nature (Stewart et al., 2017). Upon diagenesis, it can also be dissolved and recrystallized due to high alkalinity fluids in the presence of reduced sulphur complexes (Kerr et al., 2017). Thus, ore textures and gold chemistry are not always reliable for investigating the primary source of gold and there is a need to find other, more reliable evidence. Other heavy minerals are transported alongside gold in the sedimentary environment and they can provide alternative and auxiliary evidence. Classically, pyrite has been used in such studies, but it is prone to oxidation and dissolution under diagenetic conditions (Schieber, 2007).

Another common heavy mineral found in placers is rutile (tetragonal TiO_2), an important accessory mineral in both felsic and mafic rocks that mainly forms during low to high-grade metamorphism (Meinhold, 2010) and is widely found as a detrital mineral in sedimentary rocks (Morton and Hallsworth, 1994). It endures chemical and physical weathering and it can preserve its original features at low to medium metamorphic grade conditions (Meinhold, 2010). As a versatile tool, rutile has been used in many different studies, such as a monitor of Nb and Ta fractionation processes during high-pressure metamorphism and melting (Marschall et al., 2013), as a geothermometer of high-grade metamorphism (*e.g.* Meyer et al., 2011), and as an ore indicator, associated to gold mineralisation (*e.g.* Scott and Radford, 2007). Concentrations of W, Fe, Sb and V have been proposed as a discriminating proxy for identifying Au-related rutiles (Clark and Williams-Jones, 2004). A complementary approach in discriminating sources resides in the study of mineral inclusions. Hart et al. (2016, 2018) have recently used mineral inclusions in rutile and compared with those of the host rocks to introduce a new tool for retrieving P-T information enclosed in detrital minerals. Because of the ubiquity of detrital rutile in the sedimentary record, this approach could be particularly useful as a provenance tool and in assessing the nature of detrital gold.

Here, we report new evidence on the gold source of a small and restricted quartz-pebble conglomerate type gold deposit from the Paleoproterozoic Minas Supergroup, Quadrilátero Ferrífero (QF), Brazil by using detrital rutiles and their inclusions. With a prolonged

metamorphic, magmatic and hydrothermal history, the origin of the gold in the Au-U-bearing horizons of the Moeda Formation is a source of controversy (comparable to that of the Witwatersrand deposit), as multiple gold generation events can be tracked in the QF (Vial et al., 2007d) and evidence of the detrital character of the gold has somehow been lost (Pires, 2005). This has led to contrasting models of modified placer versus hydrothermal origin being currently debated (Koglin et al., 2012; Pires, 2005; Minter et al., 1990).

Combining mineralogical information such as texture, inclusions and chemistry is a powerful tool that, in this study, has been applied to unravelling the nature of gold source and recycling. Together with reliable rutile U-Pb ages, the data reconcile gold sources in the Moeda Formation to those from the Archean greenstone belt through sedimentary recycling.

1.1 Rutile in Earth Sciences

Titanium dioxide has many polymorphs, but mainly three occur in nature: rutile, anatase and brookite. Rutile and anatase crystallize in the tetragonal system in different space groups, while brookite crystallizes in the orthorhombic system.

Rutile can grow in a range of environments, including by solid state reactions during metamorphism, and as precipitates in melts and fluids (Force, 1980; Okamoto and Maruyama, 2004; Choukroun et al., 2005; Scott and Radford, 2007; Rapp et al., 2010). Authigenic growth of rutiles can also occur in sedimentary rocks (e.g. Mader, 1980). Substitution of Ti in rutile by minor elements is controlled by the size, valency and crystal field effects of the substituting element (Scott, 2005). These can include elements such as Ta, Nb, Fe, Sn, Cr, Cu, V, Sb, W and Zr. This results in rutile being an important controller of trace elements in the continental crust, such as Nb and Ta.

Rutile can also incorporate Zr and Hf, and they have been shown to be temperature-dependent and, in the case of Zr, calibrated as a geothermometer (*e.g.* Zack et al., 2004). The Zr-in-rutile geothermometer has been widely applied in many studies (*e.g.* Meyer et al., 2011; Kooijman et al., 2012; Pape et al., 2016; Hart et al., 2016). However, Chen and Li (2008) and Cabral et al. (2015) have shown difficulties with its application at either UHP

metamorphic conditions or low-grade metamorphic conditions, respectively. Hart et al. (2016) demonstrate how the use of mineral inclusions can help constrain pressure, and thus assist in temperature estimates, while Shulaker et al. (2015) presented a new calibration at lower temperature ranges combined with oxygen isotopes. Regardless, this has been a useful tool in complementing P-T-t constraints and more studies are needed to tackle these existing difficulties. For useful reviews of rutile applications and more detailed information, see Meinhold (2010) and Zack and Kooijman (2017).

Despite a significant occurrence of rutile associated with metallic ore deposits (Williams and Cesbron, 1977; Rice et al., 1998; Clark and Williams-Jones, 2004), there are relatively few publications related to hydrothermal rutile compared with metamorphic rutile. Rutile from mesothermal and related gold deposits has been reported to contain W, and variable amounts of Sb and V. In addition, it incorporates Ni and Cu if related to magmatic-hydrothermal Pd-Ni-Cu deposits, and in W-Sn deposits associated with granite-pegmatites it incorporates W, Sn, and high concentrations of Nb and Ta (Clark and Williams-Jones, 2004). Molybdenum found in hydrothermal porphyry Cu–Mo rutiles has shown temperature- and sulfur activity- dependence (Rabbia et al., 2009). This variety of trace elements in rutile has been useful in distinguishing hydrothermal from metamorphic rutile and as ore indicators. Since rutile can also incorporate trace amounts of U, U-Pb isotopic analyses can be applied to determine mineralisation ages (Richards et al., 1988; Machado et al., 1992; Pi et al., 2017).

1.2 Mineral inclusion considerations

Mineral inclusion studies in robust minerals have been shown to offer new insight into mantle and crust-forming processes. However, these have mainly focussed on diamond, zircon, chromite and garnet as host minerals (e.g. Harris, 1972; McCammon et al., 1998; Ye et al., 2000; Hutchison et al., 2001; Tian et al., 2011; Shatsky et al., 2015). However, new avenues are being explored, with recent studies investigating rutile as a mineral inclusion carrier (Hart et al., 2016; 2018).

The application of mineral inclusion studies in detrital minerals has been increasing, but still account for less than 10% of the published mineral inclusion studies. Yet, much insight about early Earth geology has come mainly from detrital zircon studies (e.g. Jack Hills

zircons; Hopkins et al., 2010), with provenance studies based on the occurrence of certain detrital heavy minerals, their proportions and geochemistry (e.g. Morton and Hallsworth, 1994; Zack et al., 2004). Complementing these with detailed mineral inclusion studies will lead to a better characterisation of sources and understanding of their magmatic, metamorphic and tectonic significance.

Fluid inclusions have been classified as *primary*, when solitary or isolated and usually of large size; *pseudosecondary*, forming during mineral growth and usually following trails constrained by the host crystallography (both forming with the host mineral); and *secondary*, post-dating mineral growth (Roedder, 1984; Bodnar, 2003). These definitions have been revisited by gemmologists, especially with respect to diamond studies, and a different terminology can be applied: p*rotogenetic* for solid inclusions older than the host, *syngenetic* for inclusions formed with the mineral host, and *epigenetic* for solid inclusions formed after (Taylor et al., 2000; 2016; Nestola et al., 2017). However, the term *primary* is still widely used to refer to mineral inclusions that are older or co-genetic with their host (*e.g.* Bell, 2016). We shall use the same approach, and term primary for both older and co-genetic inclusions, and secondary for inclusions postdating the host.

While in magmatic or metamorphic systems, defining the primary origin of an inclusion is relatively straightforward, in hydrothermal systems assignment is more difficult. Because hydrothermal systems can be long-lived and with multiple fluid pulses, mineral growth is more sluggish and intricate, as previously highlighted by Wilkinson (2001). Whenever mineral inclusions are in clear association with fractures or at the edges of the host-mineral, they can be assigned as secondary inclusions. However, precipitation after dissolution can also lead to the development of isolated inclusions, easily perceived as primary (Fig. 1). Recent experiments show how these are usually circumscribed to the edges of reacting grains or are controlled by the host crystallography (Putnis, 2002; Harlov et al., 2005; Spruzeniece et al., 2017).

In the present study, we aim to discuss the nature of mineral inclusions in the light of these different processes. Since it is extremely difficult to distinguish protogenetic inclusions from syngenetic phases or even re-precipitation micro-inclusions, they shall be addressed hereafter, and at the first instance, as primary inclusions.

2. Geological Setting and Gold Mineralisation

2.1 Geological Setting

The QF is located in the south-easternmost portion of the São Francisco Craton (SFC), representing part of the South American Platform (Fig. 2). The QF encompasses Paleo- to Mesoarchean Tonalite-Trondhjemite-Granodiorite (TTG) suites, Neoarchean high-K granitoids, an Archean greenstone belt (Rio das Velhas Supergroup), and a Paleoproterozoic supracrustal sequence (Minas Supergroup), unconformably overlain by a Paleoproterozoic sedimentary sequence (Itacolomi Group). Complex poly-phase deformation in the region has resulted in a dome-and-keel structure, where the domes are dominated by the Archean crystalline basement, and the keels by the supracrustal sequences (Alkmim and Marshak, 1998).

The TTG crust was generated during three main magmatic growth periods from 3220 until 2770 Ma (Lana et al., 2013). These are the Santa Bárbara (SB; 3220-3200 Ma), Rio das Velhas I (RVI; 2930-2900 Ma) and Rio das Velhas II (RVII; 2800-2770 Ma) events. The Archean crust was intruded by voluminous granitoids in two pulses: Mamona event I (MI), between 2750 and 2700 Ma, and Mamona event II (MII) between 2620 and 2580 Ma (Farina et al., 2015). The Rio das Velhas Supergroup (RdV) is juxtaposed tectonically with the TTG basement and it can be subdivided into two groups (Noce et al., 2005): a basal sequence composed of mafic to ultramafic volcanic rocks interlayered with BIF, cherts, pelites and felsic volcaniclastic rocks (Nova Lima Group), and a nearshore to non-marine clastic sequence (Maquiné Group).

The Minas Supergroup was deposited unconformably over the RdV greenstone belt/crystalline basement, although locally the boundary has been reactivated and become highly tectonised (Hartmann et al., 2006). The Minas Supergroup comprises a complete sedimentary record of a Wilson cycle, developed between ca. 2600 and 2000 Ma (Alkmim and Marshak, 1998), including from bottom to top: the Caraça, Itabira, Piracicaba and Sabará groups (Dorr, 1969, Renger et al., 1995).

The Caraça Group consists of the stratigraphically-oldest Moeda Formation, an alluvial sandstone sucession containing conglomeratic and pelitic intercalations, which grades upwards into shallow-water marine pelites comprising the Batatal Formation. The deposition age of the Moeda Formation has been debated in the literature, with suggestions

of 2580 Ma (Hartmann et al., 2006), 2610 Ma (Martínez Dopico et al., 2017), 2650 Ma (Machado et al., 1996), and 2680 Ma (Koglin et al., 2014).

According to Machado et al. (1992), during the Paleoproterozoic Minas orogeny, the QF was subjected to amphibolite facies metamorphism, which has been supported by U-Pb isotopic studies of titanite and monazite (Aguilar Gil et al., 2017), and P-T conditions were high enough to result in partial melting of the Archean crust, as suggested by recent work from Carvalho et al. (2017). Pires (2005) identified a peak metamorphic assemblage in the supracrustal units of the Moeda and Batatal formations compatible with greenschist facies metamorphism, including the presence of muscovite + kyanite.

The QF units are intruded by pegmatitic veins and mafic dykes, the former yielding monazite U-Pb ages of 2060 Ma (Noce, 1995) and the latter yielding baddeleyite U-Pb ages of 1798 Ma (Cederberg et al., 2016) and 1714 Ma (Silva et al., 1995; Cederberg et al., 2016).

Gold has been found associated with hydrothermal alteration zones in the Nova Lima Group in the RdV, in the basal conglomerates of the Moeda Formation and in veins hosted by different units within the Minas Supergroup. Isotopic ages associated with these gold mineralising events range from Neoarchean to Neoproterozoic, and a summary can be found in Supplementary material A.

2.2 Gold mineralisation hosted in the Archean greenstone belt

Gold mineralization in the QF is mostly hosted by banded iron formations (BIF), mafic volcanics and quartz veins associated with the Nova Lima Group (Lobato et al., 2001; Ribeiro-Rodrigues et al., 2007). These are structurally controlled, as the hydrothermal fluids were channelled along deformation zones (Baltazar and Zucchetti, 2007). To these authors, gold mineralisation took place between 2750 Ma and 2670 Ma associated with a collisional tectonic setting. The timing of this gold mineralisation event is still debated, but the best available U-Pb age using gold-related monazite yields an age of 2672 Ma (Lobato et al., 2007).

Gold can be anhedral, included in the sulphides, or occurring as thin films, filling fractures. In most gold deposits, the Au:Ag ratio varies from 5:1 to 6:1 (Lobato et al., 2001). The same authors noticed that gold grades generally increase with As-enrichment in pyrite or

pyrrhotite. In the Morro Velho world-class deposit (470 metric tons cumulative production), the sulphide assemblage comprises pyrrhotite (74%), arsenopyrite (17%), pyrite (8%) and chalcopyrite (1%).

Cubanite, sphalerite, galena, tetrahedrite and ullmannite occur as minor phases. Associated oxides include magnetite, ilmenite, rutile and leucoxene. Other phases are also common, such as apatite, fluorite, and scheelite, as well as various carbonates and silicates (Vial et al., 2007a). Both oxygen and sulphur isotopes of sulphides imply a metamorphic or juvenile (magmatic) source for these ore fluids (Vial *et al.* 1987; 2007a). Microthermometric fluid inclusions suggest gold precipitation temperatures between 300 and 375 °C (Morales et al., 2016).

2.3 Au-U mineralisations hosted in the Moeda Formation

The conglomerates in the Moeda Fm. often occur in paleo-valleys, reaching thicknesses of a few metres. They are mostly composed of quartz-pebbles, although there are also schist-pebbles, in a sandy matrix with some sericite. Wallace (1958) subdivided the Moeda Fm. in its type area (Moeda syncline, western QF) into unit I, II and III. According to Villaça and Moura (1981) and Villaça (1981) the basal unit I is characterized by a sequence of metaconglomerates that grade up and laterally into coarse- and medium-grained quartzites. This unit ranges from 50 to 180 m in thickness. The matrix is predominantly sericitic, locally pyrite-rich and/or carbonaceous. Some horizons are uraniniferous with vein-quartz pebbles, while others are polymictic with quartz-vein, quartzite and schist pebbles. Unit II is made up of interlayered phyllites and fine quartzites with strong lateral variation, with thicknesses ranging from 0 to 70 m. Pires (2005) suggested these two units are part of the same, lower depositional sequence. Unit III disconformably overlies the lower sequence and consists of basal polymict metaconglomerate grading upwards into medium- and fine-grained quartzites that total about 200m in thickness. This represents the base for the upper sequence of Pires (2005). The Moeda Fm. is commonly unconformably or tectonically juxtaposed against the greenstone belt, except on the western side of the QF, in the Moeda syncline, where it unconformably overlies the TTG basement.

The highest gold grades are usually restricted to the contact with the greenstone belt, in places that have been interpreted as proximal alluvial fan settings, constrained by significant topography. The most significant gold grades occur in the Gandarela and Ouro Fino

synclines, to the east of the Bação Complex (Scarpelli, 1991; Pires, 2005). According to these authors, the higher gold grades are also in close proximity to shear zones and in the vicinity of significant carbonaceous-rich layers. Minter et al. (1990) showed the gold composition and grade to be very similar to that of the Witwatersrand deposit, with gold concentrations varying between 1.45 and 19.75 ppm, with an average of 7.6 ppm, whilst U concentrations are about 79 ppm. This is in accordance with an earlier report on the economic potential of those conglomeratic lenses, which can reach several grams per ton of gold, but are not economically viable to mine (Pomerene, 1964). Although free gold particles can be found, with an abraded detrital texture, most gold occurrences within the Moeda Fm. are related to post-depositional pyrite, in equilibrium with chlorite and pyrophyllite. Gold usually occurs as inclusions in skeletal pyrite, as in-fills of pyrite fractures, or in association with pyrite overgrowths (Pires, 2005; Koglin et al., 2010).

Koglin et al. (2012) also noted that gold could form aggregates with tourmaline, cross-cutting pre-existing compact detrital pyrite. Furthermore, the gold-related chlorite compositions suggest high Fe-Mg protoliths, with a composition indicative of formation temperature around 300°C (Pires, 2005). This author suggests that the evidence supports either a hydrothermal origin for the gold in the Moeda Fm., or a very strong remobilization of the detrital gold during later orogenic events, such as the Paleoproterozoic or the Neoproterozoic in age deformation events. However, based on textural evidence, Koglin et al. (2012) suggest a hydrothermal origin instead.

3. Sampling and Analytical Methods

3.1 Samples and sample preparation

Samples used in this study are the same as those in Martinez-Dopico et al. (2017), except for one sample that was also collected from the western flank of the Moeda syncline (Fig. 1). These comprise three samples of unit I, two of unit III, and one sample assigned to unit III, although stratigraphic controls were weak. These have all been metamorphosed at greenschist facies conditions, as discussed in section 2.1. From unit I, one sample corresponds to the Au-U conglomerate (AA01) and two to the overlying sandstone (4517 and 4524). As for the other samples, assigned to unit III, one sample comes from the basal conglomerate unit (4522) and the other two from the overlying sandstone units (4520 and 4518). Detrital zircon geochronology and implications for the deposition age of the Moeda Formation were presented by Martinez-Dopico et al. (2017).

For details concerning sample description, preparation and heavy mineral separation procedures we refer to Martinez-Dopico et al. (2017) as the same samples and procedures have been used. Rutiles for this study were hand-picked and mounted in 2.5cm diameter polished epoxy resin mounts. Mounts were further polished for electron backscatter diffraction using a Buehler VibroMet with a 0.05µm size aluminium oxide suspension.

3.2 Analytical Methods

Rutile grains were investigated using a Scanning Electron Microscope (SEM) equipped with energy dispersive X-ray spectroscopy (EDS) and electron backscatter diffraction (EBSD) detectors that allowed for mineral inclusion identification, textural investigation and structural distinction of TiO_2 polymorphs. Rutiles and thin or thick sections were imaged and investigated using a ZEISS EVO10MA (SEM) with a LaB_6 electron source, a silicon drift (SDD) Oxford Instruments X-MAX (80) EDS detector and an Oxford Instruments Nordlys Nano electron EBSD hosted at the University of Portsmouth (UoP). Analytical conditions were variable, depending on the aims for each session. Data were acquired using the SMARTSEM® v.05.09 software, while the data were processed using Oxford Aztec and HKL Channel 5 software. For backscattered electron (BSE) and secondary electron (SE) imaging, an accelerating voltage of 15 kV and 200-400 pA beam current was applied. When

performing detailed and careful examination of the composition of mineral inclusions, an acceleration voltage of 10-15 kV and beam currents between 400 and 1000 pA at 14.5 WD were preferred, as these result in the generation of the highest output in counts per second, while maintaining a relatively small volume interaction (under 1µm). EBSD spot analyses were performed in different analytical sessions, using 20 kV accelerating voltage and 400-600 pA beam current, with the stage positioned at a 70° angle with respect to the beam path. These conditions work for an optimised set up, to generate the highest signal to background of the diffraction pattern (EBSP). The Oxford Aztec software includes a mineral diffraction EBSP database, from which we used rutile (Swope et al., 1995), brookite (Meagher and Lager, 1979) and anatase (Ballirano and Caminiti, 2001) diffraction data against each specimen EBSP.

Combined Electron Probe Microanalysis (EPMA) and Laser Ablation Coupled Inductively Plasma Mass Spectrometry (LA-ICPMS) allowed for minor and trace element quantification. Rutiles were analysed in a CAMECA SX100 electron probe at the University of Bristol with operating conditions of 20 kV acceleration voltage, and a beam current of 200 nA with a 2 µm electron beam. Ten elements were measured, including Si(kα) and Al(kα) to monitor interference of mineral inclusions, and then V(kα), Cr(kα), Fe(kα), Nb(Lα), Sn(Lα), Sb(Lα), Ta(Lα) and W(Lα). Ti was estimated by difference. Further trace elements in rutile were determined using an ASI RESOlution 193nm ArF excimer laser coupled to an Analytik Jena Plasma Quant Elite ICP quadrupole MS at UoP. Rutiles were ablated with laser beam diameters between 35 and 25 µm, at an energy density of ≈ 4.5 J/cm2 and at a repetition rate of 6 Hz. Analysis consisted of 20 s background, 30 s ablation and sample acquisition, and 5 s of wash out, resulting in a total analysis time of 55 s. The following isotopes were analysed: ^{49}Ti, ^{29}Si, ^{25}Mg, ^{31}P, ^{45}Sc, ^{51}V, ^{52}Cr, ^{55}Mn, ^{63}Cu, ^{66}Zn, ^{69}Ga, ^{87}Sr, ^{89}Y, ^{90}Zr, ^{93}Nb, ^{95}Mo, ^{107}Ag, ^{118}Sn, ^{121}Sb, ^{177}Hf, ^{181}Ta, ^{182}W, ^{208}Pb, ^{209}Bi, ^{232}Th and ^{238}U. A sample-standard bracketing method was used to correct for mass fractionation using NIST610 as a primary standard (using reported concentrations from Pearce *et al.,* 1997). R10 (Luvizotto et al., 2009), BCR-2 (using reported concentrations from Wilson, 1997) and NIST612 (reported concentrations from Jochum et al., 2011) were used as secondary standards, measured values being within 5-10% of published values.

U-Pb isotopic analyses on rutile were performed using an ASI RESOlution 193nm ArF excimer laser coupled to an Analytik Jena Plasma Quant Elite ICP quadrupole MS at UoP.

Analyses were performed during different analytical sessions with variable parameters such as spot sizes ranging from 30 to 50 µm, with a laser energy density between 2.5 and 3 J/cm2 and repetition rates of 3 and 5 Hz. A sample-standard bracketing method was used to correct for mass fractionation using R10 rutile as a primary standard (average ID TIMS age of 1091.3 ± 4.7 Ma; Luvizotto et al., 2009), and three different secondary standards were analysed; R13 (SIMS age of 504 ± 4 Ma; Schmitt and Zack, 2012), R19 (ID TIMS age of 493 ± 10 Ma; Zack et al., 2011) and SAE (unpublished, ID TIMS 495 Ma, provided courtesy of C. Lana, UFOP). Calculated $^{206}Pb/^{238}U$ weighted mean average ages for R13 and R19 secondary standards are within 1.2% accuracy of the reported ages.

Due to high Th concentrations and variable common-Pb (Pb_{cm}) compositions, using ^{208}Pb to correct for Pb_{cm} becomes difficult. For this reason, screening the dataset was conducted by applying a Th/U < 2 filter, which should also eliminate potential sources of non-rutile bounded Th. Pb_{cm} corrections were applied either using the ^{204}Pb- or the ^{208}Pb-based method. Detailed instrument setup, analytical methodology and Pb_{cm} correction procedures can be found in the supplementary material B.

4. RESULTS

4.1 RUTILE GRAINS AND MINERAL INCLUSIONS PETROGRAPHY

From six samples, 5970 rutile grains were hand-picked for further investigation. These include for Unit I, 379 grains from sample AA01, 1032 grains from sample 4517, and 941 grains from sample 4524; for unit 2, 599 grains from sample 4522, 1373 grains from sample 4520 and 1646 grains from sample 4518.

4.1.2 Rutile polymorphism

Trace element incorporation has been shown to vary quite significantly with TiO_2 polymorphism (Triebold et al., 2011), which may impact data interpretation. Thus, during this study, we proceeded to identify the TiO_2 polymorphs using EBSD (SEM). Multiple grains in each sample were tested, either using spot or scanning area analyses, with reference to the database included in the Oxford Instruments Aztec software (refer to section 3.2). The software compares 8 to 10 crystallographic planes from each specimen obtained from the

Kikuchi bands against the structure of rutile, anatase and brookite and calculates a mean angular deviation (MAD) between detected and simulated bands. Evaluation of MAD values allows to determine the level of confidence in each assignment. 99% of all analysed grains (ca. 100) have been positively identified as rutile, with MAD values between 0.3 and 0.4, with less than 1% of assignments corresponding to non-indexed points, resulting from the presence of mineral inclusions. No grains were assigned to anatase or brookite.

4.1.3. Rutiles and mineral inclusions from Unit I

Rutiles were examined during picking using both transmitted and reflected light microscopy to complement morphology and opacity observations. Detailed textural images and mineral inclusion identification were performed using BSE and EDS. Automated feature maps were conducted to scan across the epoxy mounts and allow rapid selection of grains for more detailed analysis.

Due to the compositional nature of certain mineral phases, the identification proposed is occasionally only indicative, as analyses are only semi-quantitative. This is especially relevant for sulphosalt minerals. These were performed using EDS semi-quantitative analyses referenced to mineralogical databases including webmineral (webmineral.com), mindata (mindata.org) and SFU (sfu.ca/~marshall/sem/spectra.html).

Regarding certain inclusions, mainly corresponding to silicate minerals, whether they are completely isolated from the matrix is dubious. Evidence suggests the presence of both isolated, neddle-shape and non-isolated cases. Compositionally, they range from mica to quartz aggregates, and they imply a secondary origin, formed after deposition of the detrital rutile “host”.

However, in the case of mineral inclusions of interest in this study, particularly due to their small size, it is most unlikely in 3D that they connect with the matrix. Thus, we will refer to them as inclusions, not specifying if they could have resulted from re-precipitation.

Sample AA01 - metaconglomerate

This sample is a strongly foliated, polymictic orthoconglomerate, with flattened quartz pebbles. Areas of small grain-size, due to deformation, have the highest concentration of gold particles (Fig. 3-I), as well as rutiles and other heavy minerals (Fig. 3-II & -III). In some areas gold particles are in equilibrium with micron-sized rutile grains (Fig. 3-IV). Grains

collected from the heavy mineral non-magnetic concentrates are rutile-rich. Overall, grains are orange in colour, very rounded in shape and on average smaller than 100 µm in diameter. Rutile grains in this sample have many different features, but a common one is the intense development of secondary mica inclusions, that cross-cut many grains (Fig. 3-V). Sulphide inclusions are not common, occurring in less than 10% of host grains. Zircon is the most common inclusion, alongside xenotime and As-rich iron oxides, probably formed after As-rich pyrite (Fig. 3-VI & -VIII). Pyrrhotite and pyrite are rare, but they can be found as very small inclusions (<3 µm; Plate 3-V & -VII). Dissolution and re-precipitation features with pore development can also be found (Plate 3-IX).

Sample 4517 – quartzite

The non-magnetic heavy mineral concentrates are rutile-rich and it is clearly the most abundant accessory mineral. Rutiles are mainly rounded to elongate and sub-spherical in shape, exhibiting a brownish red colour, with a few grains being more pale orange in colour. The lustre of some of these rutiles could be characterized as greasy to silky, most probably due to the presence of mineral inclusions. In transmitted combined with reflected light microscopy, these rutiles tend to be dark, occasionally showing a red, orange or yellow tint. On average, rutiles are 170 µm in diameter, with modal grain size between 200 and 150 µm. Zircon is the most common inclusion, followed by uranium oxide (uraninite or a related uranium-bearing oxide; Fig. 4). Monazite, xenotime and scheelite occur in similar proportions, with significant occurrence of brabantite and thorium oxide (thorite or other Th-rich oxide). Most of these minerals can be found as isolated inclusions (Fig. 5A) with considerably small grain sizes (< 5µm), except for zircon and monazite which can be up to 10s of µm. In BSE these rutiles show very fine, patchy zonation (Fig. 5A, arrows) and the development of some porosity. This porosity is frequently filled with silicate minerals (quartz or white mica).

Sample 4524 – quartzite

Rutiles are mainly rounded to elongate prisms and sub-spherical in shape; they have an amber colour. The lustre of some of these rutiles is greasy to silky, most probably due to the presence of transparent mineral inclusions. In reflected light, these rutiles show a sub-metallic lustre when exhibiting higher opacity and show a strong red colour when semi-

opaque. On average, rutiles are 130 µm in diameter, with modal grain size between 150 and 100 µm. Although the grains have similar textural features to the other samples studied, these grains have less non-silicate mineral inclusions. Chalcocite is the most abundant inclusion in this quartzite (Fig. 4), and they are usually isolated and of medium to small grain size (8-2 µm; Fig. 5B). Uranium oxide is the second most abundant inclusion, with multiple occurrences per grain (Fig. 5B). Zircon, pyrite, iron oxides, brabantite and monazite are also found as inclusions, having variable grain sizes ranging from 1 to 5 µm. Rutile grains have local porosity and patchy zoning in BSE imaging (Fig. 5B, arrows).

4.1.4. Rutiles and mineral inclusions from Unit III

Sample 4518 - quartzite

The non-magnetic heavy mineral concentrates are rutile-rich and it is the most abundant accessory mineral. Rutiles are mainly rounded to elongate and sub-spherical in shape, and they have a dark amber colour. The lustre of some of these rutiles is greasy to silky, most probably due to the presence of mineral inclusions. In transmitted light many of the grains are mostly opaque, with only a very few being semi-opaque, and showing strong orange-brown colours. On average, rutiles are 180 µm in diameter, with two clear modes: one ranges between 250 and 200 µm, and the second between 180 and 120 µm. Virtually every grain has some sort of inclusion, and every grain has on average 2 to 3 inclusions. Sulphides and sulfosalts are very common, arsenopyrite being the most common, followed by tetrahedrite and berthierite (Fig. 4). Sulphides and sulfosalts can coexist in some rutiles (Fig. 6), or with other phases, such as monazite or zircon. Pyrite, As-rich pyrite, pyrrhotite and stibnite also occur as inclusions, but not as frequently (<5%). Rutile grains show quite strong patchy zoning in BSE signal and have a porous texture (Fig. 6, arrows).

Sample 4522 - metaconglomerate

Rutiles are mainly rounded to elongate and sub-spherical in shape; they have a brownish-red colour. The grains contain inclusions, mainly of opaque minerals. The lustre of some of these rutiles occasionally is greasy to silky, again most probably due to the presence of mineral inclusions. On average, rutiles are 170 µm in diameter, with modal grain size between 200 and 150 µm. Iron oxides are the most prevailing inclusions, but they can result from the oxidation of an iron-rich sulphide phase (Fig. 7A). Zircon is the second most

abundant inclusion, followed by chromium oxide (probably chromite) (Fig. 4). The latter can have a specific arrangement in rutile, as seen in Fig. 8. Arsenopyrite and pyrite are the most common sulphide minerals included in rutile, the first up to 10s of microns in size (Fig. 7A). Patchy zoning and tiny needle-like inclusions of silicate minerals are also revealed by BSE imaging.

Sample 4520 - quartzite

The non-magnetic heavy mineral concentrates are rutile-rich. Rutiles are mainly spherical in shape and have a brownish-red or amber colour. Inclusions of mainly opaque minerals are present, which probably leads to a greasy to silky lustre of some of these rutiles. On average, rutiles are 130 µm in diameter, with modal grain size between 230 and 150 µm. Pyrite is the most common mineral inclusion, with small grain sizes (< 5µm; Fig. 7B). Pyrrhotite and zircon are the next most common, with grains up to 10s of microns in size. Other sulfosalts and phosphates occur but make up for less than 4% of the bulk of inclusions each (Fig. 4). In BSE images, patchy zoning and needle-shaped silicate mineral inclusions can be found (Fig. 7B).

4.1.5. Summary

Mineral inclusions in rutile are very common in Unit I and Unit III. A summary of the representative primary mineral inclusions occurring in each sample (Fig. 4) distinguishes the main types of inclusions occurring in this formation. Zircon is by far the most common, followed by pyrite, present in all of the samples. Interestingly, monazite that occurs as a detrital mineral in the Moeda Formation, is also a common mineral inclusion, alongside iron oxides. The latter seem to have formed due to oxidation of previous sulphide phases, as suggested by commonly high-As contents. Uraninite, thorite, chalcocite and scheelite only occur as inclusions in rutiles from Unit I. Sample 4518 should be emphasized as it records the widest variety of sulphide and sulfosalt mineral inclusions, and the highest amount both per grain and within grains. Arsenopyrite, tetrahedrite and berthierite are among the most common mineral inclusions, with the occurrence of As-rich pyrite, and these are rather frequent ore-related minerals associated with gold mineralisation in the RdV greenstone belt.

The presence of chalcocite and scheelite are noteworthy, as their occurrence is not as widespread as that of other sulphide ore-related minerals, and it could be useful in terms of provenance studies as their spatial occurrence in the basement is quite restricted.
Grain textures, such as high porosity and patchy zoning, combined with a variety of mineral inclusions, such as sulphides, sulfosalts, oxides, tungstates, phosphates and silicates contribute to establishing a primary hydrothermal origin. Rutile growth is related to As-Fe-Cu-Sb-Pb-rich mineralising fluids, and this could have followed multiple growth events, replacement of ilmenite or magnetite and/or other complex nucleation growth mechanisms. Samples show variation in the diversity and density of mineral inclusions, from Fe-Cu-As-Sb-rich (Unit III) to W-Cu-U-rich (Unit I), which can be interpreted as different sourcing of rutile within the mineralising system.
The presence of silicate inclusions, of mica and quartz composition, overprinting the rutiles is interpreted as epigenetic, and possibly related to dissolution and precipitation features preserved in some of the rutiles. Similar needle-shape mineral inclusions and textures were found in rutiles in the Gandarela syncline (QF), interpreted as authigenic (Zeh et al., 2018).

4.2 Rutile mineral chemistry

EPMA combined with LA-ICPMS allow determination of both minor and trace element concentrations of various elements in rutile. Mineral chemistry data results can be found in the supplementary material C.

4.2.1 Rutile chemistry diagrams

Rutiles from Unit I and Unit III have been plotted in the Cr vs Nb diagram (Fig. 8), to help discriminate between felsic and mafic sources. Although this diagram was originally designed to separate felsic from mafic metamorphic protoliths (Zack et al., 2004), Cr- or Nb-enrichments should also reflect mafic from more felsic lithologies along the fluid path or in its source. Some rutiles have very high enrichments in Cr or Nb, which can be used to argue in favour of fluids that either circulated through a very mafic source or a very felsic source.

In turn, many other rutiles have intermediate contents of both elements, suggesting mixing of both components. Sample 4517 has a predominance of Nb-rich rutiles, whereas the other samples have higher Cr concentrations.

Clarke and Williams-Jones (2004) highlighted the relationship between W-bearing rutile and mesothermal gold. In their study, that accounted for hundreds of samples from different types of ore deposits, rutile from unaltered wallrock in mesothermal gold deposits showed below detection limit or very low concentrations of W, while in the sub-ore or ore zone, rutile preferentially incorporates W, up to 1000s ppm. Figure 9 demonstrates the presence of W-bearing rutiles in our samples, and ca. 35% are highly enriched, and thus can clearly be linked to gold mineralisation.

From the ca. 35% of the Au-related rutiles, the majority (>80%) were from sample 4517 in Unit I, where scheelite occurs as a mineral inclusion.

Combining different trace elements to produce a variety of ternary diagrams shows that there are significant correlations between different groups of samples (Fig. 10).

Combining Ti, Nb + Fe, and Cr splits the rutile population into different groups. While rutiles from sample AA01 have apparent lower concentrations of the Ti-substituting trace elements, the remaining samples have variable composition, but higher substitution (Fig.10a). Some rutiles are more Cr-rich, whilst others are more Nb and Fe-rich. This should reflect the nature of the fluids and/or precipitation conditions, as some rutiles incorporated higher amounts of trace elements compared to others. As the Cr-Nb diagram implies, either a predominantly mafic source, felsic or a mixed source of fluids can account for the precipitation of rutile. Further discrimination between Fe and Nb highlights an interesting relationship (Fig. 10b). The population is clustered in the metamafic field, comprising most rutiles, but within the metapelitic field, there is a clear enrichment towards Fe-rich rutiles, especially considering the ones that are clearly linked to gold mineralisation. However, the mixing between Cr and Fe involves some Nb. As these two cations can have the same valence at 3+, this is a common substitution. However, since Ti is 4+, Nb with 5+ compensates for the charge balance. To understand if sourcing of these fluids has had any effect on the gold-mineralisation-related rutile growth, combining the previous cations with W should highlight it. Figure 10c shows the distribution of the population in such a diagram, combining the information of proximity to gold mineralisation. Although there is mixing evidence, the majority of the W-rich rutiles have a more pelitic signature (left side), whilst

rutiles that are more Cr-rich (right-side), even when they have elevated W concentrations, are not in the ore zone, but probably formed in alteration/sub-ore zones. It seems reasonable to infer, from the data, that Nb and Fe-rich rutile with considerable W was precipitated with gold. Vanadium and Fe correlation is strongly positive, and due to the fact that V is usually enriched in mafic igneous rocks, concentrated in titanomagnetite, together with the fact that magnetite from BIF is usually V-poor (Nadoll et al. 2014; Aronsson 2016), a discriminating plot using either Nb or Cr against V and Fe has been used (Fig. 10d). Both diagrams, either with Nb or Cr at the top apex, show a very significant clustering of rutiles from the different units from the Moeda Formation. Unit I rutiles, from samples 4517 and 4524, are clearly more Fe-rich, whereas rutiles from Unit III are enriched in V. Rutile is commonly formed after magnetite or ilmenite through epitaxial replacement, and thus if such growth took place during the gold-mineralisation events, some of the V would get incorporated into rutile. Knowing that the gold mineralisation in the RdV is mainly hosted by the BIF, and that those magnetites would be V-poor, it could explain why rutiles in close proximity to gold are Fe-rich instead. The BIF in the RdV is stratigraphically above an ultramafic to mafic sequence and is preceded by a volcaniclastic sequence of intermediate to felsic composition. This would result in the presence of both V-rich and V-poor magnetite/ilmenite, from which V-rich and V-poor rutiles grew.

4.2.2 Nb-Ta and Zr-Hf diagram

Although some studies on the Nb-Ta chemistry of hydrothermal rutile have been published, Hf data are usually not readily available (*e.g.* Clarke and Williams-Jones, 2004; Scott, 2005; Scott and Radford, 2007). Rutile Zr/Hf vs Nb/Ta data have been compiled from different rock types, including peridotites, eclogites, blueschists and garnet-mica schists, and fluid-related rutiles, including this study (Fig. 11).

Niobium and Ta ratios from the Moeda Fm. rutiles range between 2-3 and 30 and have subchondritic Zr/Hf ratios. About 82% of the rutiles have subchondritic Nb/Ta, with 60% exhibiting lower than average continental crust ratios. W-rich rutiles with determined Archean U-Pb ages are plotted as *orogenic gold-related* and they overlap significantly with published ratios of metamorphic rutile, independently of metamorphic grade. However, the latter can comprise higher, chondritic to subchondritic Zr/Hf ratios, and on average higher Nb/Ta ratios. This is in clear contrast to rutiles formed in peridotites that have

suprachondritic Zr/Hf and a wide range of Nb and Ta ratios (sub to suprachondritic ratios). Authigenic, diagenetic or post-depositional fluid-related rutile, including type 2 rutiles from Zeh et al. (2018), show a similar trend and plot in a separate field showing very low Nb/Ta values (Fig. 11).

This highlights the existence of fractionation between Nb/Ta in hydrothermal systems, and the preferential uptake of Ta over Nb by hydrothermal rutile. These results support experimental rutile/fluid and rutile/melt partitioning coefficient data for Nb and Ta (Green and Adam, 2003; Klemme et al., 2005).

Similar compositions of rutile have been found associated with granitic pegmatites, containing high Nb (several thousand ppm) and Ta (hundreds of ppm) concentrations, and low Nb/Ta ratios, reflecting variable partitioning of Nb and Ta into a fluid phase during magmatic crystallisation (Carruzzo et al., 2006).

4.2.3 Principal component analysis

To investigate the existence of major chemical vectors in the detrital rutiles from the Moeda Fm. that could help in identifying trends and variations in the population, a principal component analysis (PCA) was conducted. This also helped to make sure that no other significant chemical vector was missing from those discussed above and summarised in Fig. 11. GCDKit (Janousek et al., 2006; 2011) provides a multivariate analysis tool that conducts a PCA analysis, as well as basic statistics. Our PCA analysis uses a covariance matrix. Forty-three data points out of 275 available entries were used for this analysis. These correspond to data enclosing full mineral chemistry information, namely Nb, Ta, W, Fe, V, Cr, Sb and Ti. Because Ti is a driving vector, to see the behaviour of the dataset, two different PCAs were performed: one including Ti and another excluding it. Results of the PCA are summarized in Table 1.

The PCA shows that 99% of the variability can be explained with only 4 components in both cases. These results are comparable to a PCA including a partial dataset but incorporating more elements, of which little to no relevance was found in defining trends. When using Ti, PC1 accounts for 82% of variability, while in its absence Nb becomes predominant in PC1. Fig. 12 shows the eigenvectors for PC1 and PC2.

The four major components when Ti is absent are Cr, W, Fe, Nb (Fig. 12a), whereas when Ti is considered, Nb, Fe and Cr are significant, but W has less weight in comparison (Fig. 12b).

As expected, Ti has an opposite weight to Nb and Fe, as these compete in the structure of rutile. Interestingly, it seems that Nb and Fe explain the variability of the population in the same way. This can be interpreted as both elements being sourced from the same rock-type, and therefore the Fe content of these rutiles being explained as coming from a felsic source (Nb-rich) rather than from a more mafic source (Cr-rich) as would be predicted. This is confirmed by the strong correlation factor between Nb and Fe at 0.9.

4.3 Rutile U-Pb geochronology

U-Pb isotopic analyses were performed on rutiles by LA-ICPMS (see supplementary materials D). Concordia diagrams, weighted mean average ages and age frequency histograms were calculated using ISOPLOT/EX 4.1 (Ludwig, 2009). The rutiles all have complex internal textures and inclusion populations, but care was taken to try and analyse inclusion-free domains. Due to intricate patchy zonation, it was impossible to target the different domains at the spatial resolution needed to collect sufficient U and Pb for precise U-Pb geochronometry. However, all the analysed grains show similar textures and/or types of inclusions, and thus should be part of a single age population. Rutiles in this study have highly variable U, Th and common Pb compositions. Different common Pb corrections were applied, depending on the nature of each data point/rutile grain. Due to the complex nature of the analysed rutiles, a combination of parameters had to be implemented to achieve reasonable and sensible results. From 473 U-Pb signal integrations, 217 analyses passed the threshold of the quality filters that were applied. From these, 48 grains have no common-Pb (Pb_{cm}) within measurement uncertainty; the remaining grains required a Pb_{cm} correction, which was based on either ^{204}Pb or ^{208}Pb, as applicable. For the detailed procedure of the Pb_{cm} correction approach used in this study, see the supplementary material B. For the relative probability plots, >10% discordant grains were discarded. This filter is commonly used in detrital population studies (e.g. Lancaster et al., 2015; Moreira et al., 2016), although it allows for the inclusion of grains that might have suffered small amounts of Pb-loss.

Unit I – samples AA01, 4517 and 4524

Sample AA01 contains rutile grains with an average U concentration of 25 ± 18 ppm, while Th concentration is 13 ± 11 ppm. From 43 grains analysed, only 29 were considered for plotting and age determination based on the criteria above (Fig. 13). Two grains did not need any Pb_{cm} correction, while the remaining 27 show evidence for incorporation of Pb_{cm} and were corrected. From the 29 grains, 22 are within 10% concordance. Four of these grains cluster at 2857 ± 65 Ma ($^{207}Pb/^{206}Pb$ age). The remaining grains have a range of $^{207}Pb/^{206}Pb$ ages, but most cluster around 1800-2100 Ma, with a main peak at 2095 Ma. Sample 4517 contains rutile grains with an average U concentration of 26.5 ± 27 ppm, while Th concentration is 8 ± 11 ppm. From 109 grains analysed, 61 were selected for plotting and age determination. From these, 22 grains did not contain Pb_{cm}, while the remaining 39 showing evidence for Pb_{cm} incorporation were corrected using either the ^{204}Pb or ^{208}Pb based Pb_{cm} corrections. A subgroup of 19 Pb_{cm} free data points from this sample define a discordia with an upper intercept at 2818 ± 21 Ma and a lower intercept at 524 ± 140 Ma (Fig. 14a). Most of the ^{208}Pb-based Pb_{cm} corrected data are in close agreement with the uncorrected data, reinforcing these ages. However, some scatter in ^{204}Pb-based Pb_{cm} corrected data can be interpreted as the presence of other discordia/mixing lines, possibly reflecting the existence of other detrital ages in this sample. Despite the quality filter controls applied for the Pb_{cm} corrections, the possibility for some under- or overcorrected data should also be considered. See supplementary material A for detailed information about these filters.

Other concordant ages yielded $^{207}Pb/^{206}Pb$ ages of ca. 2798, 2846 and 2893 Ma, highlighting the presence of different detrital ages.

Sample 4524 contains rutile grains with an average U concentration of 16 ± 20 ppm, while Th concentration is 6 ± 12 ppm. From 77 analysed grains, only 26 were selected for plotting and for age determination. From these, 8 had no evidence of Pb_{cm} incorporation, while the remaining 18 had to be corrected using both ^{204}Pb and ^{208}Pb-based Pb_{cm} corrections. From these, 8 data points, including 5 with no evidence for Pb_{cm}, form a discordia with an upper intercept at 2868 ± 69 Ma and a lower intercept at 585 ± 93 Ma (Fig. 14b). Other concordant ages define $^{207}Pb/^{206}Pb$ age clusters at 2.8-3.0 Ga and at 2.6 Ga. There are other discordant grains down in the Concordia diagram that could potentially represent grains that suffered

Pb-loss yielding a different primary crystallisation age from the ones presented in the highlighted discordia line in Fig. 14b.

Unit III – samples 4522, 4520 and 4518

Sample 4522 contains rutile grains with an average U concentration of 11 ± 11 ppm, while Th concentration is 3 ± 2 ppm. From 57 analyses, only 24 were selected for plotting and age determination. From these, only 5 showed no evidence for the incorporation of Pb_{cm}. Two concordant age clusters occur at about 2758 ± 77 Ma and 2413 ± 92 Ma while the remaining concordant data range from 1.8 to 2.2 Ga. Combining Pb_{cm} free data with Pb_{cm} corrected data, a discordia with an upper intercept at 2750 ± 42 Ma and a lower intercept at 412 ± 36 Ma (Fig. 14c) can be defined.

Sample 4520 contains rutile grains with an average U concentration of 3.4 ± 2 ppm, while Th concentration is 0.8 ± 1 ppm. From 62 analyses, 29 were able to be Pb_{cm} corrected. The majority of the data are restricted to between 1.8 and 2.2 Ga, while a couple of analyses are concordant at ca. 2485 Ma and 2746 Ma ($^{207}Pb/^{206}Pb$ ages).

Sample 4518 contains rutile grains with an average U concentration of 8 ± 9 ppm, while Th concentration is 5 ± 6 ppm. From 138 analyses, 56 were selected for plotting and age determination. From these, 15 showed no evidence for incorporation of Pb_{cm}. Many analyses are close to concordant, ranging from 2.4 to 3 Ga, while some discordant data can represent either Pb-loss or an underestimation of Pb_{cm}. Some of the Pb_{cm} corrected and naturally Pb_{cm} absent data were combined as they form a discordia with an upper intercept at 3011 ± 36 Ma and a lower intercept at 302 ± 150 Ma (Fig. 14d).

Samples from different units within the Moeda Fm. show agreement in terms of their geochronology, although some subtle differences exist. In Unit I, the presence of concordant data and upper intercept ages confirm the detrital nature of these rutiles, with ages spanning from 2818 to 2868 Ma, i.e. older than the maximum deposition age. Two samples from Unit III show concordant age data and an upper intercept age at 2750 Ma, again confirming the detrital nature of these rutiles. Sample 4518 shows some older inheritance, with concordant data and an upper intercept age at 3011 ± 36 Ma. There are also two

clusters of ages: one at 2690 ± 90 Ma and a second one at 2580 ± 80 Ma; A third, less pronounced cluster age, occurs at 2790 ± 72 Ma.

It is clear from the combined data that there is a strong Pb-loss event at about 600-400 Ma, which is in agreement with reworking of the crust during the Brasiliano deformation event. Not as obvious, due to the overprint of this younger Pb-loss event, is an older tectono-metamorphic event responsible for the total or partial resetting of rutile ages to 1.8 and 2.1 Ga; this is particularly more significant in samples AA01 and 4520. These ages are in agreement with reported ages of the Minas orogenic event that affected the QF.

Combining previously published detrital zircon and the new rutile U-Pb data to investigate the potential sources of these rutiles has been done using >90% concordant data, including <10% reversely discordant data (Fig. 15). Due to large uncertainties on the $^{207}Pb/^{206}Pb$ ages associated with error propagation from Pb_{cm} corrections, frequency histograms are presented without the relative probability density curve which dilutes geological variability. Overall, the rutiles have coincident age peaks with some of the zircon main age peaks, implying similar processes and sources for both detrital mineral species (Fig. 15a and c). This is sometimes masked by uncertainties in the U-Pb age determination and propagated Pb_{cm} corrections. However, rutiles frequently have younger ages (Fig.15 a and b), which can be explained by the lower U-Pb closure temperature in rutile and therefore resetting of the original age to some extent, by diffusional Pb-loss and/or dissolution-precipitation of rutile. In sample 4517, the main rutile age populations reflect growth between the RVI and RVII events, whereas in the upper unit (sample 4518), rutiles seem to be slightly younger, formed during the MI and MII events, compatible with its zircon population. Sample 4520 and 4522 have poor preservation of their detrital sources, with determined U-Pb ages showing elevated reworking during the Paleoproterozoic Minas orogeny between 2.1 and 1.9 Ga.

5. Discussion and Conclusions

5.1. Rutile mineral chemistry, mineral inclusions and growth implications

In hydrothermal systems, the presence of TiO_2 minerals has usually been ascribed to anatase, as it is considered to be a lower temperature and pressure stable polymorph

(Smith et al. 2009). However, these same authors showed that anatase can be metastable at all temperatures, very dependent on water, pressure and impurities. This study reinforces the stability of rutile at low P-T conditions (see section 2 for P-T estimates). Due to its ubiquity in the analysed samples, hydrothermal systems should be considered as important contributors to the rutile budget.

Despite recent attention paid to rutile, both as an exploration tool (Scott et al., 2011) and as a key mineral to enlighten crustal processes (*e.g.* Gao et al., 2014), the detailed study of their inclusions to further constrain P-T conditions and/or source is only in the waning stage (Hart et al., 2016; 2018) compared to zircon (*e.g.* Darling et al., 2009).

Rutiles found in the Moeda Fm. have a systematic occurrence of mineral inclusions, including a range of silicates, sulphides, sulfosalts, tungstates, phosphates and oxides. Combined with grain texture and porosity, this has helped to establish a primary hydrothermal origin. These relationships also raise questions with respect to the oxidation conditions of fluids that led to rutile precipitation/replacement, with the presence of both oxides and sulphides.

Uranium and thorium oxide inclusions seem to be associated with scheelite mineral inclusions in rutiles sourced to Unit I only. About 35% of the rutile population show W-enrichment, particularly in sample 4517, with rutiles showing the highest W concentrations, linking them to gold mineralisation. Further investigation highlighted higher Fe-Nb contents in these gold-mineralising-related rutiles, potentially indicating a felsic Fe-rich host sequence interacting with these mineralising fluids. These can be affiliated to the Archean BIF that hosts most of the gold occurrences in the greenstone belt (Lobato et al., 2001).

Rutiles from Unit III have different mineral inclusion populations, strongly dominated by sulphides, namely pyrite, pyrrhotite, arsenopyrite, and berthierite. These sulphides have been associated with gold mineralisation in the greenstone belt (Vial et al., 2007a) and have not be found in the matrix of the members of the Moeda Fm., except for pyrite. Favourably, similar mineral inclusions have been found in detrital pyrite (Minter et al., 1990). Although many rutiles from this unit have considerable Nb concentrations, they are more Cr-rich than the ones from Unit I. Their W contents are lower in comparison to sample 4517 but are high enough to associate them with the gold precipitation processes, related to the sub-ore and alteration zones.

Unit III rutiles are enriched in V in comparison to Unit I. Although the presence of V in rutile associated with porphyry Cu-Au and mesothermal gold deposits has been noted (Clark and Williams-Jones, 2004), W does not show any correlation with V. Therefore, it is not clear if these elements were in competition in such settings. Vanadium in rutile has been described as being redox-dependent (Liu et al., 2014). In their findings, Nb and V show a negative correlation, interpreted to reflect oxygen fugacity controls in the V oxidation state. In oxidising conditions, there is more Nb^{5+} in rutile, and because V^{5+} has a lower affinity for rutile, its incorporation is reduced. However, in the rutiles from this study, V-Nb show a positive correlation (r^2=0.92). As an alternative solution, we propose that rutile formed as a replacement after magnetite/ilmenite in the host rock. Fluid-mediated mineral replacement is common in hydrothermal settings. Depending on the V concentration in magnetite, which reflects its magmatic or metasomatic derivation (Nadoll et al. 2014), epitaxial rutile could scavenge significant V. This hypothesis would also satisfy the largely immobile nature of V during metamorphism and metasomatism.

Rutiles in the Moeda Fm. show a wide range of Nb/Ta ratios, extending to very low ratios (<6), and relatively similar Zr/Hf compared to metamorphic rutile. Orogenic gold-related rutile (W-rich, with sulphide inclusions and Archean ages) show a significant overlap in Nb/Ta values with metamorphic rutile, which is consistent . These observations are supported by recent data from similar rutiles from the Gandarela syncline in the QF, where fluid-assisted precipitation of rutile led to similar ratios (Zeh et al., 2018). The scatter in these ratios has been noted before in eclogites, yet rutile average ratios mimic the whole-rock Nb/Ta (Zack et al., 2002). In hydrothermal systems, many other mineral phases are in competition for a number of elements, and thus the lower Nb/Ta could reflect such processes, either by Ta being liberated from a dissolved mineral phase or Nb being incorporated by a competing mineral phase. For instance, Ta is more readily incorporated into augite and titanite than Nb. Degradation of the former, during metamorphism, could lead to the release of Ta into metamorphic fluids. Alternatively, this could also reflect a higher partitioning coefficient of Ta over Nb in rutile in these systems, which is suggested by experiments (Green and Adam, 2003).

It should be noted that Nb/Ta of Archean continental crustal rocks could have been lower than in the present and has been proposed as having an average of 6 (Wedepohl, 1991). This ratio is consistent with the ratios found in a good number of these rutiles, and

significantly lower than the post-Archean equivalents. If these rutiles reflect to some extent the Nb/Ta of their host-rocks/crustal fluids, then this could be used to source the ore fluids and the host-rock that interacted with those fluids, to Archean or post-Archean crust.

The presence of thorite (or Th-oxide), possible uraninite (or U-oxide), as well as chromium- and zirconium-oxides should be carefully discussed. It has been shown experimentally that monazite can precipitate from an apatite-host during metasomatism (Harlov et al., 2005), both being phosphatic minerals. Usually, re-precipitation is associated with an infiltration front, typically responsible for porosity development (Putnis, 2002; Harlov et al., 2005) and exsolution of some components from the host, combined with the fluid chemistry. Element exsolution and mineral precipitation has been discussed in the literature as being due to adjustments to different P-T conditions and oxygen fugacity (Sun et al., 2007; Yamamoto et al., 2009; Alifirova et al., 2015). Because rutiles from this study show a complex chemistry, it is likely that excess Th, U, Cr and Zr at a certain oxygen partial pressure and temperature could be exsolved from the interstices or from the lattice of rutile after rutile growth or from a Ti-Fe oxide precursor during rutile growth in the presence of a supersaturated fluid (Seydoux-Guillaume et al., 2002; 2012; Grand'Homme et al., 2017). Evidence for rutile-hematite being stable and precipitating from hydrothermal fluids indicates fluid oxidising conditions (Buddinton and Lindsley, 1964; Rečnik et al., 2015). However, the widespread occurrence of sulphides and sulfosalts suggests more reducing conditions.

Xenotime occurs frequently associated with zircon, and in most cases replacing it, and thus it is considered a secondary product of alteration (Finch et al., 2001; Franz et al., 2015). Monazite, on the other hand, occurs as variable size, isolated and non-isolated inclusions. It also occurs as a detrital mineral in the same unit. Monazite is sparingly soluble in most geological conditions, yet its solubility increases with increased oxygen fugacity (Trail, 2018). Fluid-mediated experiments at different temperatures show that even at low temperatures (ca. 300 °C) secondary monazite can precipitate with a different composition from primary monazite (Seydoux-Guillaume et al., 2012). Our observations are thus compatible with co-precipitation of monazite and rutile from a supersaturated fluid whose redox conditions swung between more oxidising and more reducing during prolonged growth. This is compatible with field observations from gold-lode veins in the greenstone belt showing variations in the redox conditions during gold precipitation (Morales et al., 2016).

5.2. Au-related rutiles and U-Pb geochronological implications

Except for sample AA01, free gold particles or rutiles containing gold inclusions were not found in the investigated samples. Also, as previously noted by Koglin et al. (2012), gold particles in the Moeda Fm. show hydrothermal textures, intergrown with tourmaline that cross-cuts detrital pyrite. However, this could be the result of Proterozoic crustal circulation of hydrothermal fluids. Gold particles are quite soft and susceptible to remobilisation and recrystallization. Recrystallization and overgrowth of gold particles is enhanced by grain deformation attained during transport and can occur during diagenesis (Stewart et al., 2017). This leads to a complete transformation of the grain surface, and loss of morphological detrital features. Besides, neutral or slightly alkaline aqueous fluids combined with the presence of thiosulphate (oxidation of primary and authigenic pyrite) are enough to remobilize gold in the sediments and lead to the mobilisation of silver out of the gold particles, changing the original gold composition (Stewart et al., 2017). In this way, it is reasonable to propose that the interaction of such fluids with the detrital gold in the Moeda Fm. could have led to its remobilization. Additionally, recent experiments conducted by Tanis et al. (2016) showed the influence of fluid composition in rutile solubility and how it is more effective than temperature. Thus, complex aqueous fluids, such as a combination of NaCl, KCl and/or NaF (+B), can dissolve rutile components, especially at temperatures higher than diagenesis. Such complex fluid chemistries have been reported from the Ouro Fino syncline (QF), where quartz-hematite and sulphide-quartz veins that cross-cut the Minas Supergroup have fluid inclusions with low pH, high sulphate concentration, and high CO_2-N_2 volatiles (Boiron et al., 1999). These fluids are further characterised by low Na/K, variable Cl/SO_4, with high Na/Ca, B, Li and F with high fO_2. This can, to some extent, be supported by the disturbed U-Pb system in rutiles (temperature-dependent) and could be accounted for by dissolution, recrystallization, gold remobilization and re-precipitation with tourmaline in aggregates. Such aggregates have been described in gold-tourmaline vein deposits hosted in the Minas sequence, such as at Passagem de Mariana, attributed to the Brasiliano orogenic event (Vial et al., 2007b). However, no tourmaline inclusions have been found in rutiles from the Moeda Fm.

Variable amounts of Pb_{cm}, combined with two young Pb-loss events, if not also ancient Pb-loss events during the Archean, makes the U-Pb dataset quite difficult to interpret.
In the Moeda Fm. we have found inherited rutile ages, older than the maximum deposition age, as well as reset ages between 2.1 and 1.8 Ga. This resetting has been recorded in rutiles from the same unit but to the east of the QF and was accompanied by new authigenic rutile growth (Zeh et al., 2018). There is also a younger Pb-loss event between 600 and 450 Ma, responsible for the partial resetting of many rutiles, which has also been reported by Zeh et al. (2018).

The age of the gold mineralisation in the RdV greenstone belt is not yet clear from our dataset. One area of ambiguity arises from the overall large uncertainties associated with the U-Pb dating of these rutiles, while another arises from the apparent spread of Archean ages. All rutiles show similar textures and similar primary inclusions, which suggests a similar geological setting. Yet, sample 4518 contains detrital rutiles which have abundant sulphide inclusions and have different ages (outside of analytical uncertainty). In this sample, rutiles yielding ca. 2.7 Ga ages contain arsenopyrite, pyrite and tetrahedrite, sulphides with a strong affinity to the gold mineralisation. The detrital rutile population in sample 4517 is somewhat similar, with the main age peaks spanning the RVI to RVII events, and significant rutile growth during MI event (refer to section 4).
These data suggest distinctive episodes of hydrothermal activity in the RdV greenstone belt. During these multiple hydrothermal activity events, the gold must have been remobilised and concentrated in the Archean crust, lasting up to the end of the Mamona II event.
Another hypothesis to explain these data is that some rutiles were already present in the Rio das Velhas crust at the time of the ore fluid circulation and that some rutiles suffered complete resetting, where temperatures were higher, while most rutiles precipitated from the fluid itself or formed after ilmenite or magnetite as a replacement reaction. This could account for the presence of different Archean ages, with some grains showing ancient Pb-loss while others retained the original age. A combination of both should also be considered.

Au-related rutiles in this study have high Nb and Ta concentrations, sometimes unusually high (see section 4.2.1). As already discussed, W-rich rutiles with such compositions have

been reported from fluids originated from granite-pegmatites (Carruzzo et al., 2006). Although most fluid inclusion studies from the Archean lode-gold ore-bodies have reported a dominant metamorphic fluid source (Morales et al., 2016), a recent B-isotopic study has reported mixing between magmatic and metamorphic fluids being responsible for tourmaline formation, associated with late Archean granitoid intrusion (Albert et al., 2018). Although not widespread in the RdV, tourmalines have been found as part of the gangue mineral assemblage, including rutile, associated with ore minerals (Vial et al., 2007c; Brumal deposit). Therefore, we propose similar mixing for the precipitation of these Au-related rutiles. This reinforces the contribution of fluids generated during the MI event as partially responsible for Au-remobilisation and precipitation.

Although detrital zircons have slightly different age peaks, some can be associated with the rutile ages. The younger 2.2 to 1.8 Ga and ca. 500 Ma ages in rutile are not present in zircons, which can be explained as due to the much lower Pb-closure temperature in rutile. Some sample bias in detrital zircon studies, during selection of suitable grains that optically show no evidence of metamictization, could also account for this dissimilarity.

Temperatures attained during the Minas and Brasiliano orogenic events that affected the western flank of the Moeda syncline were not high enough (greenschist facies) to disturb the U-Pb system in zircon but were more than sufficient to cause partial Pb-loss in rutile. This was probably enhanced by relatively small grain sizes (frequently below 100 μm) and high porosity. As a final remark, it is clear that the Brasiliano deformation front propagated at least to the Moeda syncline during the tectono-metamorphic events.

5.2.1. Significance of 2.2 to 2.6 Ga U-Pb ages

It is clear from our U-Pb dataset, considering $^{207}Pb/^{206}Pb$ ages, that there is a widespread occurrence of ages between 2.2 and 2.6 Ga. From 31 analyses, 25 are <10% discordant ($^{206}Pb/^{238}U/^{207}Pb/^{206}Pb$ ages). Of these, 16 are >98% concordant. Sample AA01 exhibits a higher proportion of these ages, compared to the other samples (ca. 27% of concordant ages). These ages, mostly around 2.25 Ga, have also been recently reported in rutiles in the Gandarela syncline (Zeh et al., 2018).

To help understand the significance of such ages, U-Pb isotopic ratios of both $^{206}Pb/^{238}U$ and $^{207}Pb/^{235}U$ have been modelled to reflect different degrees of mixing between a younger age

at 2.0 and 2.1 Ga, and an older age at 2.66 and 2.72 Ga. This set of ages are chosen due to: a) being consistently represented in the analysed rutile population; b) the oldest ages corresponding to the main source for the detrital zircon population; c) corresponding to meaningful ages found all around the QF, the youngest corresponding to the collisional and collapse stages of the Paleoproterozoic Minas orogeny, and the oldest corresponding to two important Archean crustal components of the QF, respectively.

For the modelling, U concentration of both components, decay constants, average uncertainties for the measured isotopic ratios, and degree of mixing were used as intensive parameters. Two case scenarios were assumed for U concentrations: a) to be similar; b) the young component having 30% less than the older component. This allows estimation of the degree of mixing in both scenarios and tests how it affects the final age. In the case of similar concentrations, the degree of mixing can be compared to a degree of Pb-loss, as the latter is independent of U concentration.

For the same degree of mixing, comparing both U/Pb isotopic ratios allows determination of the degree of concordance. For all the scenarios, final ages between 2.0 and 2.72 resulted in concordance within 98% (Fig. 16). Variations in the U concentration are reflected highly in the degree of mixing for a given age. For instance, a 2302 Ma age with the same end-member U concentrations indicates mixing of 70% from a 2100 Ma constituent, and the remaining from a 2660 Ma component. The same example, but with the younger end-member having 70% U concentration of the older component, requires the participation of 50% of each age component.

Thus, we can explain similar dates as a result of mixing between two components with similar concentration or as multiple degrees of mixing of different concentration components. Highly concordant dates can also reflect Pb-loss during the selected period and are easily masked by Pb_{cm} combined with large uncertainties. This observation is sympathetic with natural geological variability.

Combining the results from this modelling with the large uncertainties associated with these isotopic measurements (and propagated after Pb_{cm} corrections) ascertains the validity of interpreting these 2.2 to 2.6 Ga dates as a result of either Pb-loss or/and mixing between newly grown rutile at 2.0/2.1 Ga and inherited detrital rutile at 2.66/2.72 Ga. Both scenarios are supported by evidence recorded in rutiles from this study. This is especially true for the

basal conglomerate unit, showing higher degrees of alteration during the Paleoproterozoic Minas orogenic event.

5.3. The Au-U-bearing horizons of the Moeda Formation in a wider geodynamic context

The global orogenic gold event that characterizes the late Archean can be recognised in several cratons such as the Superior Province and the Yilgarn Craton (Goldfarb et al., 2001). These gold ore-forming events mainly occurred at about 2630 Ma, but some ages range from 2670 to 2600 Ma (in Goldfarb et al., 2001), similar to the orogenic lode gold in the RdV greenstone belt. Analogous Witwatersrand-type deposits of Paleoproterozoic age have been found elsewhere (Whymark and Frimmel, 2017), related to the Superia Craton. These Superia-related basins were interpreted to have formed during the rifting of Kenorland, before 2480 Ma (Whymark and Frimmel, 2017). It is extremely likely that the Minas basin was part of such a geodynamic setting, including the development of these widespread orogenic-gold events, that preceded the extensional tectonics which led to the opening of these basins, and the subsequent formation of gold placers recorded in these detrital sequences. In the Elliot Lake Group, detrital rutile is found alongside pyrite, gold and uraninite, where the ore minerals show signs of remobilisation or authigenic growth (Roscoe, 1996). Similarly, the Matinenda Fm. (Huronian Supergroup) also has signs of fluid circulation at around 2.1 and later at 550 Ma, disturbing the U-Pb system of kerogen grains found in the gold-bearing units (Mossman et al., 1993). The presence of detrital pyrite and uraninite with gold is ubiquitous in all these sequences, and it has been used to define the sedimentation as being older than the Great Oxidation Event GOE. The transport and deposition of pyrite but especially uraninite was only possible at <1% of the present atmospheric level (PAL; Ono, 2001).

Rutiles from Unit I show, consistently, the presence of uranium and thorium oxides, while rutile from Unit III lack such inclusions. Instead, the presence of As-rich Fe-oxides inclusions in such rutiles increases. These observations may reflect variations in the source of these rutiles, as rutiles from 4517 have a different age distribution to those from unit III. The transition from unit II to unit III is represented in the sedimentary record by the deposition of a basal conglomerate unconformably over unit II. This suggests early readjustments of the newly-formed rift basin, which could account for this variation in source. In addition, the

deposition of the Moeda Fm. occurred during the atmospheric transition into a slightly higher atmospheric oxygen level, which could have prevented uraninite from reaching the basin as easily as during the deposition of unit I. Gumsley et al. (2017) suggest the waning stages for this rise in atmospheric oxygen level occurred at 2.46 – 2.42 Ga. This is in excellent agreement with a carbonate Pb-Pb age from the Itabira Group, capping the Caraça Group, at 2420 Ma (Babinski et al., 1995) concomitant with the GOE-related BIF precipitation that can be correlated with other Paleoproterozoic basins.

The similarities between the Moeda and the Paleoproterozoic sequences found in the Superia Craton, with respect to sedimentological, tectonometamorphic and magmatic events, is striking. Yet, the ca. 2.45 Ga volcanic event that precedes these Superia-related sequences (Bleeker, 2003; Whymark and Frimmel, 2017) is absent in the SSFC. This magmatic episode occurred at a global scale, but not all land-masses were affected by it (Bleeker, 2003). The South American cratons have also shown similarities to the southern hemisphere cratonic blocks (Bleeker, 2003; Teixeira et al., 2007), and yet, the chronology of events, types of sequences, magmatism and metamorphism between the Slave and the SF craton makes it favourable to hypothesize an affinity to the Sclavia clan, including cratons such as Dharwar and Zimbabwe. All these different affinities seem to favour a partial shared geodynamic evolution between all the Archean blocks. This joint evolution could have started at the end of the late Archean, with the formation of Kenorland (Bleeker, 2003). The Kenorland solution encompassing all the three major cratonic clans coexisting in a single supercontinent could explain stratigraphic and metallogenetic resemblances between the Moeda and many of the Paleoproterozoic sequences found in the Superia Craton, but at the same time reconcile it with the strong affinity with the Sclavia clan blocks. Dissimilarities between these in terms of chronology of events and magmatism could be explained as due to diachronism in the evolution of continents, and geological heterogeneity in the processes behind cratonization and intracontinental rifting such as the one observed during the rifting of Pangea (Marzoli et al., 2018).

5.4 Concluding remarks

This study shows the suitability of detrital rutile as a powerful tool to elucidate processes and provenance, combining isotopic U-Pb and mineral chemistry with detailed mineral inclusion petrography.

U-Pb data yield ages older than the maximum deposition age (> 2.58 Ga), supporting the detrital nature of these rutiles. The range of rutile U-Pb ages combined with large uncertainties does not allow better constraints on the age of Archean gold mineralisation. However, combining the results arising from this study with constraints known for the lode-gold mineralisation, we suggest a prolonged mineralising event during the late Archean, culminating with the cratonization and collapse stages of the SSFC and Mamona events (Fig. 17a). Gold precipitated mostly in pyrite, arsenopyrite and pyrrhotite, alongside monazite, rutile and other sulphides (Martins Pereira et al., 2007). Upon precipitation in a relatively shallow environment, the gold-bearing rocks were weathered and a range of heavy minerals were transported by alluvial fans into an intracratonic basin during the early stages of the Paleoproterozoic (Fig. 17b). Detrital rutiles were sourced from different levels of this mineralised crust, as testified by variations both in mineral chemistry and in mineral inclusion populations.

Two significant tectonometamorphic events affected the SSFC: the Paleoproterozoic Minas and the Neoproterozoic Brasiliano events. Rutiles were partially or greatly affected by these events, with both U-Pb age resetting and authigenic growth at ca. 2.1 Ga during the Minas event, the first stage of gold remobilisation. This was assisted by a large-scale hydrothermal circulation capable of remobilising great amounts of gold in the Minas Supergroup. Complex fluid chemistry and low pH are behind the dissolution and reprecipitation of rutile, pyrite and gold (Fig. 17c). At ca. 500 Ma, during the Brasiliano reworking event, another episode of hydrothermal circulation reportedly remobilised gold leading to its precipitation as lode-gold veins higher in the basin sequence, associated with tourmaline (Fig. 17c). Hence, this study supports a modified placer model for the gold-bearing horizons of the Moeda Formation. These fluid-assisted gold remobilisation events can be found in other correlated Paleoproterozoic gold-bearing horizon units that represent the rifting of the presumable Kenorland Supercontinent.

ACKNOWLEDGMENTS

We would like to thank Drs. Stephanie Lasalle, Stuart Kearns and Benjamin Buse for all the support and teachings during both LA-ICPMS and EPMA analyses. Professor Randall Parrish useful comments and help with the U-Pb dating and modelling are greatly appreciated. Many thanks go to Joseph Dunlop for all the support during SEM sessions and fruitful discussions. Geoff Long is also thanked for sample preparation. We also appreciate useful discussions with colleague Hugo Moreira, Professor Fernando F. Alkmim and Dr. Horst Marschall which have helped us building up some key ideas, and the comments from an anonymous reviewer that improved our manuscript. We are thankful to the University of Portsmouth for funding I. Pereira PhD research project.

REFERENCES

Aguilar Gil, C., Alkmim, F.F., Lana, C., Farina, F., 2017. Paleoproterozoic assembly of the São Francisco craton, SE Brazil: new insights from U-Pb titanite and monazite dating. Precambrian Research 289, 95–115.

Albert, C., Lana, C., Gerdes, A., Schannor, M., Narduzzi, F., Queiroga, G., 2018. Archean magmatic-hydrothermal fluid evolution in the Quadrilátero Ferrífero (SE Brazil) documented by B isotopes (LA MC-ICPMS) in tourmaline. Chemical Geology 481, 95-109. https://doi.org/10.1016/j.chemgeo.2018.02.002

Alifirova, T. A., Pokhilenko, L.N., Korsakov, A. V., 2015. Apatite, SiO<inf>2</inf>, rutile and orthopyroxene precipitates in minerals of eclogite xenoliths from Yakutian kimberlites, Russia. Lithos 226, 31–49. https://doi.org/10.1016/j.lithos.2015.01.020

Alkmim, F.F., Marshak, S., 1998. Transamazonian Orogeny in the Southern São Francisco Craton, Minas Gerais, Brazil: Evidence for Paleoproterozoic collision and collapse in the Quadrilátero Ferrífero. Precambrian Research 90, 29–58.

Aronsson, J., 2016. Compositional variations between hydrothermal and magmatic magnetite and their potential for mineral exploration using till from Laver, Northern Sweden. MSc Thesis (unpublished), Göteborg University, Sweden p.47.

Babinski, M., Chemale Jr., F., Van Schmus, W.R., 1995. The Pb/Pb age of the Minas Supergoup carbonate rocks, Quadrilátero Ferrífero, Brazil. Precambrian Research 72, 235–245.

Ballirano P., Caminiti R., 2001. Rietveld refinements on laboratory energy dispersive X-ray diffraction (EDXD) data. Journal of Applied Crystallography 34, 757-762 https://doi.org/10.1107/S0021889801014728

Baltazar, O.F., Zucchetti, M., 2007. Lithofacies associations and structural evolution of the Archean Rio das Velhas greenstone belt, Quadrilátero Ferrífero, Brazil: A review of the setting of gold deposits. Ore Geology Reviews 32, 471–499. https://doi.org/10.1016/j.oregeorev.2005.03.021

Bell, E.A., 2016. Preservation of primary mineral inclusions and secondary mineralization in igneous zircon: a case study in orthogneiss from the Blue Ridge, Virginia. Contributions to Mineralogy and Petrology 171, 1–15.

Bleeker, W., 2003. The late Archean record: a puzzle in ca. 35 pieces. Lithos 71, 99–134.

Bodnar, R.J., 2003. Introduction to Fluid Inclusions in I. Samson, A. Anderson, D. Marshall (Eds) Fluid Inclusions-Analysis Interpretations, Mineralogical Association of Canada 32, 81–99. https://doi.org/10.2138/rmg.1984.12.1

Boiron M.C., Moissette A., Cathelineau M., Banks D., Monnin C., Dubessy J., 1999. Detailed determination of palaeofluid chemistry: an integrated study of sulphate-volatile rich brines in quartz veins from Ouro Fino (Brazil). Chemical Geology 154, 179–92.

Buddinton, A.F., Lindsley, D.H., 1964. Iron-titanium oxide minerals and syntetic equivalent. Journal of Petrology 5, 310–357. https://doi.org/10.1093/petrology/5.2.310

Cabral, A.R., Rios, F.J., de Oliveira, L.A.R., de Abreu, F.R., Lehmann, B., Zack, T., Laufek, F., 2015. Fluid-inclusion microthermometry and the Zr-in-rutile thermometer for hydrothermal rutile. Geologische Rundschau 104, 513–519.

Carruzzo, S., Clarke, D.B., Pelrine, K.M., MacDonald, M. a., 2006. Texture, composition, and origin of rutile in the South Mountain Batholith, Nova Scotia. Canadian Mineralogist 44, 715–729. https://doi.org/10.2113/gscanmin.44.3.715

Carvalho, B.B., Janasi, V.A., Sawyer, E.W., 2017. Evidence for Paleoproterozoic anatexis and crustal reworking of Archean crust in the São Francisco Craton, Brazil: A dating and isotopic study of the Kinawa migmatite. Precambrian Research 291, 98–118. https://doi.org/10.1016/j.precamres.2017.01.019

Cederberg, J., Söderlund, U., Oliveira, E.P., Ernst, R.E., Pisarevsky, S.A., 2016. U-Pb baddeleyite dating of the Proterozoic Pará de Minas dyke swarm in the São Francisco craton (Brazil) – implications for tectonic correlation with the Siberian, Congo and

North China cratons. GFF 138, 219–240. https://doi.org/10.1080/11035897.2015.1093543

Chapman, R.J., Leake, R.C., Moles, N.R., Earls, G., Cooper, C., Harrington, K., Berzins, R., 2000. The application of microchemical analysis of alluvial gold grains to the understanding of complex local and regional gold mineralization: A case study in the Irish and Scottish Caledonides. Economic Geology 95, 1753–1774. https://doi.org/10.2113/gsecongeo.95.8.1753

Chen, Z., Li, Q., 2008. Zr-in-rutile thermometry in eclogite at Jinheqiao in the Dabie orogen and its geochemical implications Chinese Science Bulletin 53, 768. https://doi.org/10.1007/s11434-008-0006-1.

Choukroun, M., O'Reilly, S.Y., Griffin, W.L., Pearson, N.J., Dawson, J.B., 2005. Hf isotopes of MARID (mica-amphibole-rutile-ilmenite-diopside) rutile trace metasomatic processes in the lithospheric mantle. Geology 33, 45–48. https://doi.org/10.1130/G210841.1

Clark, J.R., Williams-Jones, A.E., 2004. Rutile as a potential indicator mineral for metamorphosed metallic ore deposits. Divex 7, 18.

Darling, J., Storey, C., Hawkesworth, C., 2009. Impact melt sheet zircons and their implications for the Hadean crust. Geology 37, 927–930. https://doi.org/10.1130/G30251A.1

Dhuime, B., Hawkesworth, C.J., Cawood, P.A., Storey, C.D., 2012. A Change in the Geodynamics of Continental Growth 3 Billion Years Ago. Science 335, 1334–1337.

Dorr, J.V.N II, 1969. Physiographic, stratigraphic and structural development of the Quadrilátero Ferrífero, Minas Gerais, Brazil. U.S. Geological Survey Professional Paper 641-A, p. 1–110.

Farina, F., Albert, C., Lana, C., 2015. The Neoarchean transition between medium and high-K granitoids: clues from the Southern São Francisco Craton (Brazil). Precambrian Research 266, 375–394.

Finch, R.J., Hanchar, J.M., Hoskin, P.W.O., Burns, P., 2001. Rare-earth elements in sinthetic zircon: Part 2. A single crystal X-ray study of xenotime substitution. American Mineralogist 86, 681–689. https://doi.org/10.2138/am-2001-5-608

Force, E.R., 1980. The provenance of rutile. Journal of Sedimentary Petrology 50, 485–488

Franz, G., Morteani, G. Rhede, D., 2015. Xenotime-(Y) formation from zircon dissolution–precipitation and HREE fractionation: an example from a metamorphosed phosphatic

sandstone, Espinhaço fold belt (Brazil). Contributions to Mineralogy and Petrology 170, 37. DOI . 10.1007/s00410-015-1191-y.

Frimmel, H.E., 2005. Archaean atmospheric evolution: Evidence from the Witwatersrand gold fields, South Africa. Earth-Science Reviews 70, 1–46. https://doi.org/10.1016/j.earscirev.2004.10.003

Frimmel, H.E., 2014. A Giant Mesoarchean Crustal Gold - enrichment Episode: Possible Causes and Consequences for Exploration in Karen D. Kelley, Howard C. Golden (Eds) Building Exploration Capability for the 21st Century, Society of Economic geology Special Publication 18, 209–234. https://doi.org/10.5382/SP.18.10

Gao, X.Y., Zheng, Y.F., Xia, X.P., Chen, Y.X., 2014. U-Pb ages and trace elements of metamorphic rutile from ultrahigh-pressure quartzite in the Sulu orogen. Geochimica et Cosmochimica Acta 143, 87–114. https://doi.org/10.1016/j.gca.2014.04.032

Goldfarb, R.J., Groves, D.I., Gardoll, S., 2001. Orogenic gold and geologic time: A global synthesis. Ore Geology Reviews 18, 1–75. https://doi.org/10.1016/S0169-1368(01)00016-6

Goto, K.T., Sekine, Y., Suzuki, K., Tajika, E., Senda, R., Nozaki, T., Tada, R., Goto, K., Yamamoto, S., Maruoka, T., Ohkouchi, N., Ogawa, N.O., 2013. Redox conditions in the atmosphere and shallow-marine environments during the first Huronian deglaciation: Insights from Os isotopes and redox-sensitive elements. Earth and Planetary Science Letters 376, 145–154. https://doi.org/10.1016/j.epsl.2013.06.018

Grand'Homme, A., Janots, E., Seydoux-Guillaume, A.M., Guillaume, D., Magnin, V., Hövelmann, J., Höschen, C., Boiron, M.C., 2017. Mass transport and fractionation during monazite alteration by anisotropic replacement. Chemical Geology 1–18. https://doi.org/10.1016/j.chemgeo.2017.10.008

Green, T.H., Adam, J., 2003. Experimentally-determined trace element characteristics of aqueous fluid from partially dehydrated mafic oceanic crust at 3.0 GPa, 650-700°C. European Journal of Mineralogy 15, 815–830. https://doi.org/10.1127/0935-1221/2003/0015-0815

Gumsley, A.P., Chamberlain, K.R., Bleeker, W., Söderlund, U., de Kock, M.O., Larsson, E.R., Bekker, A., 2017. Timing and tempo of the Great Oxidation Event. Proceedings of the National Academy of Sciences 114, 1811–1816. https://doi.org/10.1073/pnas.1608824114

Harlov, D.E., Wirth, R., Förster, H.J., 2005. An experimental study of dissolution-reprecipitation in fluorapatite: Fluid infiltration and the formation of monazite. Contributions to Mineralogy and Petrology 150, 268–286. https://doi.org/10.1007/s00410-005-0017-8

Harris, J.W., 1972. Black material on mineral inclusions and in internal fracture planes in diamond. Contributions to Mineralogy and Petrology 35, 22–33. https://doi.org/10.1007/BF00397374

Hart, E., Storey, C., Bruand, E., Schertl, H.-P., Alexander B.D., 2016. Mineral inclusions in rutile: a novel recorder of HP-UHP metamorphism. Earth and Planetary Science Letters 446, 137-148.

Hart, E., Storey, C., Harley, S.L., Fowler, M., 2018. A window into the lower crust: Trace element systematics and the occurrence of inclusions/intergrowths in granulite-facies rutile. Gondwana Research 59, 76-86. https://doi.org/10.1016/j.gr.2018.02.021.

Hartmann L.A., Endo I., Suita M.T.F., Santos J.O.S., Frantz J.C., Carneiro M.A., Naughton N.J., Barley M.E., 2006. Provenance and age delimitation of Quadrilátero Ferrífero sandstones based on zircon U–Pb isotopes. Journal of South American Earth Sciences 20, 273–285.

Hopkins, M.D., Harrison, T.M., Manning, C.E., 2010. Constraints on Hadean geodynamics from mineral inclusions in >4Ga zircons. Earth and Planetary Science Letters 298, 367–376. https://doi.org/10.1016/j.epsl.2010.08.010

Hutchison, M.T., Hursthouse, M.B., Light, M.E., 2001. Mineral inclusions in diamonds: Associations and chemical distinctions around the 670-km discontinuity. Contributions to Mineralogy and Petrology 142, 119–126. https://doi.org/10.1007/s004100100279

Janoušek, V., Farrow, C.M., Erban, V., 2006. Interpretation of whole-rock geochemical data in igneous geochemistry: introducing Geochemical Data Toolkit (GCDkit). Journal of Petrology 47, 1255–1259.

Janoušek, V., Farrow, C.M., Erban, V., Trubač, J., 2011. Brand new Geochemical Data Toolkit (GCDkit 3.0): is it worth upgrading and browsing documentation? (Yes!). Geol výzk Mor Slez 18, 26–30.

Jochum, K.P., Weis, U., Stoll, B., Kuzmin, D., Yang, Q., Raczek, I., Enzweiler, J. 2011. Determination of reference values for NIST SRM 610-617 glasses following ISO

guidelines. Geostandards and Geoanalytical Research, 35 (4): 397–429 DOI 10.1111/j.1751-908X.2011.00120.x

John, T., Klemd, R., Klemme, S., Pfänder, J.A., Hoffmann, J.E., Gao, J., 2011. Nb-Ta fractionation by partial melting at the titanite-rutile transition. Contributios to Mineralogy and Petrology 161, 35–45. https://doi.org/10.1007/s00410-010-0520-4

Kalfoun, F., Ionov, D., Merlet, C., 2002. HFSE residence and Nb/Ta ratios in metasomatised, rutile-bearing mantle peridotites. Earth and Planetary Science Letters 199, 49–65. https://doi.org/10.1016/S0012-821X(02)00555-1

Kerr, G., Malloch, K., Lilly, K., Craw, D., 2017. Diagenetic alteration of a Mesozoic fluvial gold placer deposit, southern New Zealand. Ore Geology Reviews 83, 14–29. https://doi.org/10.1016/j.oregeorev.2016.12.018

Kirk, J., Ruiz, J., Chesley, J., Titley, S., Walshe, J., 2001. A detrital model for the origin of gold and sulfides in the Witwatersrand basin based on Re-Os isotopes. Geochimica et Cosmochimica Acta 65, 2149–2159. https://doi.org/10.1016/S0016-7037(01)00588-9

Klemme, S., Prowatke, S., Hametner, K., Günther, D., 2005. Partitioning of trace elements between rutile and silicate melts: Implications for subduction zones. Geochimica et Cosmochimica Acta 69, 2361–2371. https://doi.org/10.1016/j.gca.2004.11.015

Koglin, N., Cabral, A. R., Brunetto, W.J., Vymazalová, A., 2012. Gold-tourmaline assemblage in a Witwatersrand-like gold deposit, Ouro Fino, Quadrilátero Ferrifero of Minas Gerais, Brazil: The composition of gold and metallogenic implications. Neues Jahrbuch fur Mineralogie - Abhandlungen 189, 263–273. https://doi.org/10.1127/0077-7757/2012/0223

Koglin, N., Frimmel, H.E., Minter, W.E.L., Brätz, H., 2010. Trace-element characteristics of different pyrite types in Mesoarchaean to Palaeoproterozoic placer deposits. Mineralia Deposita 45, 259–280. https://doi.org/10.1007/s00126-009-0272-0

Koglin, N., Zeh, A., Raphael, A., Augusto, A., Gomes, S., Vasconcelos, A., Neto, C., José, W., Galbiatti, H., Cabral, A.R., Gomes, A.A.S., Neto, A.V.C., Brunetto, W.J., Galbiatti, H., 2014. Depositional age and sediment source of the auriferous Moeda Formation, Quadrilátero Ferrífero of Minas Gerais, Brazil: New constraints from U–Pb–Hf isotopes in zircon and xenotime. Precambrian Research 255, 96–108. https://doi.org/10.1016/j.precamres.2014.09.010

Kooijman, E., Smit, M.A., Mezger, K., Berndt, J., 2012. Trace element systematics in granulite facies rutile: implications for Zr geothermometry and provenance studies. Journal of Metamorphic Geology, 30: 397-412. doi:10.1111/j.1525-1314.2012.00972.x

Lana, C., Alkmim, F.F., Armstrong, R., Scholz, R., Romano, R., Nalini, H.A., 2013. The ancestry and magmatic evolution of Archaean TTG rocks of the Quadrilátero Ferrífero province, southeast Brazil. Precambrian Research, 231: 157–173.

Lancaster, P.J., Storey, C.D., Hawkesworth, C.J., 2015. The Eoarchaean foundation of the North Atlantic Craton. Geological Society, London, Special Publications 389, 261–279. https://doi.org/10.1144/SP389.11

Lipson, R., 2014. The promise and perils of porphyry deposits in the future of gold production. Society of Economic Geology Newsletter, 98 (1): 11-15.

Liu, L., Xiao, Y., Aulbach, S., Li, D., Hou, Z., 2014. Vanadium and niobium behavior in rutile as a function of oxygen fugacity: Evidence from natural samples. Contributions to Mineralogy and Petrology 167, 1–22. https://doi.org/10.1007/s00410-014-1026-2

Lobato, L.M., Ribeiro-Rodrigues, L.C., Vieira, F.W.R., 2001. Brazil's premier gold province. Part 11: Geology and genesis of gold deposits in the Archean Rio das Velhas greenstone belt, Quadrilátero Ferrifero. Mineralia Deposita 36, 249–277. https://doi.org/10.1007/s001260100180

Lobato, L.M., Santos, J.O.S., McNaughton, N.J., Fletcher, I.R., Noce, C.M., 2007. U-Pb SHRIMP monazite ages of the giant Morro Velho and Cuiabá gold deposits, Rio das Velhas greenstone belt, Quadrilátero Ferrífero, Minas Gerais, Brazil. Ore Geology Reviews 32, 674–680. https://doi.org/10.1016/j.oregeorev.2006.11.007

Lorand, J.P., Gregoire, M., 2010. Petrogenesis of Fe-Ti oxides in amphibole-rich veins from the Lherz orogenic peridotite (Northeastern Pyrénées, France). Contributios to Mineralogy and Petrology 160, 99–113. https://doi.org/10.1007/s00410-009-0468-4

Ludwig, K.R., 2009. Isoplot 4.1. A geochronological toolkit for Microsoft Excel. Berkeley Geochronology Center Special Publication 4, p.76.

Luvizotto, G.L., Zack, T., Meyer, H.P., Ludwig, T., Triebold, S., Kronz, A., Münker, C., Stockli, D.F., Prowatke, S., Klemme, S., Jacob, D.E., von Eynatten, H., 2009. Rutile crystals as potential trace element and isotope mineral standards for microanalysis. Chemical Geology 261, 346–369. https://doi.org/10.1016/j.chemgeo.2008.04.012

Machado, N., Noce, C.M., Ladeira, E.A., Belo de Oliveira, O., 1992. U-Pb geochronology of Archean magmatism and Proterozoic metamorphism in the Quadrilátero Ferrífero, southern São Francisco craton, Brazil. Geological Society of America Bullettin, 104: 1221–1227.

Machado, N., Schrank, A., Noce, C.M., Gauthier, G. 1996. Ages of detrital zircon from Archean-Paleoproterozoic sequences: Implications for Greenstone Belt setting and evolution of a Transamazonian foreland basin in Quadrilátero Ferrífero, southeast Brazil. Earth and Planetary Science Letters, 141: 259–276.

Mader, D., 1980. Authigener Rutil im Buntsandstein der Westeifel. Neues Jahrburch für Mineralogie, Monatshefte 3, 97–108.

Marschall, H.R., Dohmen, R., Ludwig, T., 2013. Diffusion-induced fractionation of niobium and tantalum during continental crust formation. Earth and Planetary Science Letters 375, 361–371. https://doi.org/10.1016/j.epsl.2013.05.055

Martínez Dopico, C.I., Lana, C., Moreira, H.S., Cassino, L.F., Alkmim, F.F., 2017. U–Pb ages and Hf-isotope data of detrital zircons from the late Neoarchean-Paleoproterozoic Minas Basin, SE Brazil. Precambrian Research 291, 143–161. https://doi.org/10.1016/j.precamres.2017.01.026

Martins Pereira, S.L, Lobato, L.M., Ferreira, J.E., Jardim, E.C., 2007. Nature and origin of the BIF-hosted São Bento gold deposit, Quadrilátero Ferrífero, Brazil, with special emphasis on structural controls. Ore Geology Reviews, 32, 571-595.

Marzoli A., Callegaro, S., Jacopo Dal Corso, J.D., Davies, J. H. F. L., Chiaradia, M., Youbi, N., Bertrand, H., Reisberg, L., Merle, R., Jourdan, F. 2018. The Central Atlantic Magmatic Province (CAMP): A Review. In: Tanner L. (eds) The Late Triassic World. Topics in Geobiology, vol 46. Springer, Cham.

Mathur, R., Gauert, C., Ruiz, J., Linton, P., 2013. Evidence for mixing of Re-Os isotopes at <2.7Ga and support of a remobilized placer model in Witwatersrand sulfides and native Au. Lithos, 164-167, 65-73. DOI: 10.1016/j.lithos.2012.11.015

McCammon, C.A., Chinn, I.L., Gurney, J.J., McCallum, M.E., 1998. Ferric iron content of mineral inclusions in diamonds from George Creek, Colorado determined using Mossbauer spectroscopy. Contributions to Mineralogy and Petrology 133, 30–37.

Meagher, E.P., Lager, G.A., 1979. Polyhedral thermal expansion in the TiO2 polymorphs: Refinement of the crystal structures of rutile and brookite at high temperature Sample at 25 degrees C. The Canadian Mineralogist, 17, 77-85

Meinhold, G., Anders, B., Kostopoulos, D., Reischmann, T., 2008. Rutile chemistry and thermometry as provenance indicator: an example from Chios Island, Greece. Sedimentary Geology 203, 98–111.

Meinhold, G., 2010. Rutile and its applications in earth sciences. Earth Science Reviews 102, 1–28. https://doi.org/10.1016/j.earscirev.2010.06.001

Meyer, M., John, T., Brandt, S., Klemd, R., 2011. Trace element composition of rutile and the application of Zr-in-rutile thermometry to UHT metamorphism (Epupa Complex, NW Namibia). Lithos 126, 388–401. https://doi.org/10.1016/j.lithos.2011.07.013

Minter, W.E.L., Renger, F.E., Siegers, A., 1990. Early Proterozoic gold placers of the Moeda Formation within the Gandarela Syncline, Minas Gerais, Brazil. Economic Geology 85, 943–951. https://doi.org/10.2113/gsecongeo.85.5.943

Morales, M.J., Figueiredo e Silva, R.C., Lobato, L.M., Gomes, S.D., Gomes, C.C.C.O., Banks, D. A., 2016. Metal source and fluid-rock interaction in the Archean BIF-hosted Lamego gold mineralization: Microthermometric and LA-ICP-MS analyses of fluid inclusions in quartz veins, Rio das Velhas greenstone belt, Brazil. Ore Geol. Rev. 72, 510–531. https://doi.org/10.1016/j.oregeorev.2015.08.009

Moreira, H., Lana, C., Nalini, H.A., 2016. The detrital zircon record of an Archaean convergent basin in the Southern São Francisco Craton, Brazil. Precambrian Research 275, 84–99. https://doi.org/10.1016/j.precamres.2015.12.015

Morton, A. C., Hallsworth, C. R., 1994. Identifying provenance-specific features of detrital heavy mineral assemblages in sandstones. Sedimentary Geology 90, 241–256.

Mossman, D. J., Nagy, B., Davis, D. W., 1993. Hydrothermal alteration of organic matter in uranium ores, Elliot Lake, Canada: Implications for selected organic-rich deposits. Geochimica et Cosmochimica Acta 57 (14), 3251-3259. https://doi.org/10.1016/0016-7037(93)90538-8.

Mukhopadhyay, J., Mishra, B., Chakrabarti, K., De, S., Ghosh, G., 2016. Uraniferous paleoplacers of the Mesoarchean Mahagiri Quartzite, Singhbhum craton, India: Depositional controls, nature and source of 3.0 Ga detrital uraninites. Ore Geology Reviews, 72: 1290–1306.

Nadoll P., Angerer T., Mauk J.L., French D., Walshe J., 2014. The chemistry of hydrothermal magnetite: a review. Ore Geology Reviews, 61: 1–32.

Nestola, F., Jung, H., Taylor, L.A., 2017. Mineral inclusions in diamonds may be synchronous but not syngenetic. Nature Communications 8, 1–6. https://doi.org/10.1038/ncomms14168

Noce, C.M., 1995. Geocronologia dos eventos magmáticos, sedimentares e metamórficos na região do Quadrilátero Ferrífero, Minas Gerais. Unpubl. PhD Thesis, Instituto de Geociências Universidade de São Paulo, São Paulo, 129 p.

Noce, C.M., Zucchetti, M., Baltazar, O.F., Armstrong, R., Dantas, E.L., Renger, F.E., Lobato, L.M., 2005. Age of felsic volcanism and the role of ancient continental crust in the evolution of the Neoarchean Rio das Velhas greenstone belt (Quadrilatero Ferrífero, Brazil): U-Pb zircon dating of volcaniclastic graywackes. Precambrian Research, 141: 67–82.

Okamoto, K., Maruyama, S., 2004. The eclogite-garnetite transformation in the MORB+H2O system. Physics of the Earth and Planetary Interiors 146, 283–296.

Ono, S., 2001. Detrital uraninite and the early Earth's atmosphere: SIMS analyses of uraninite in the Elliot lake district and the dissolution kinetics of natural uraninite. PhD thesis, Pennsylvania State University, USA, p.196. https://etda.libraries.psu.edu/catalog/5900

Ono, S., Fayek, M., 2011. Decoupling of O and Pb isotope systems of uraninite in the early Proterozoic Conglomerates in the Elliot Lake district. Chemical Geology 288, 1–13. https://doi.org/10.1016/j.chemgeo.2010.03.015

Pape, J., Mezger, K., Robyr, M., 2016. A systematic evaluation of the Zr-in-rutile thermometer in ultra-high temperature (UHT) rocks. Contributions to Mineralogy and Petrology 171. https://doi.org/10.1007/s00410-016-1254-8

Pearce, N.J.G., Perkins, W.T., Westgate, J.A., Gorton, M.P., Jackson, S.E.C., Neal, R., Chenery, S.P. 1997. A compilation of new and published major and trace element data for NIST SRM 610 and NIST SRM 612 glass reference materials, Geostandards Newsletter, 21: 115–144.

Phillips, G.N., Powell, R., 2015. Hydrothermal alteration in the Witwatersrand goldfields. Ore Geology Reviews 65, 245–273. https://doi.org/10.1016/j.oregeorev.2014.09.031

Pi, Q., Hu, R., Xiong, B., Li, Q., Zhong, R., 2017. In situ SIMS U-Pb dating of hydrothermal rutile: reliable age for the Zhesang Carlin-type gold deposit in the golden triangle region, SW China. Mineralia Deposita, 52: 1179–1190.

Pires, P. 2005. Gênese dos depósitos auríferos em metaconglomerados da Formação Moeda, Quadrilátero Ferrífero, MG: o papel do Metamorfismo e associação com a matéria carbonosa. PhD Thesis (unpublished), University of Campinas, Brazil. p.209.

Pomerene, J.B., 1964. The geology and ore deposits of the Belo Horizonte, Ibirité and Macacos quadrangles, Minas Gerais, Brazil. US Geological Survey Prof Paper 341-D. 57p.

Putnis, A., 2002. Mineral replacement reactions: from macroscopic observations to microscopic mechanisms. Mineralogical Magazine, 66 (5): 689-708. doi: https://doi.org/10.1180/0026461026650056

Rabbia, O.M., Hernández, L.B., French, D.H., King, R.W., Ayers, J.C., 2009. The El Teniente porphyry Cu-Mo deposit from a hydrothermal rutile perspective. Mineralia Deposita 44, 849–866. https://doi.org/10.1007/s00126-009-0252-4

Rapp, J.F., Klemme, S., Butler, I.B., Harley, S.L., 2010. Extremely high solubility of rutile in chloride and fluoride-bearing metamorphic fluids: an experimental investigation. Geology, 38: 323–326.

Rasmussen, B., Buick, R., 1999. Redox state of the Archean atmosphere: Evidence from detrital heavy minerals in ca. 3250–2750 Ma sandstones from the Pilbara Craton, Australia. Geology 27 (2): 115–118. doi: https://doi.org/10.1130/0091-7613(1999)027<0115:RSOTAA>2.3.CO;2

Rečnik, A., Stanković, N., Daneu, N., 2015. Topotaxial reactions during the genesis of oriented rutile/hematite intergrowths from Mwinilunga (Zambia). Contributions to Mineralogy and Petrology 169. https://doi.org/10.1007/s00410-015-1107-x

Renger, F. E., Noce, C.M., Romano, A.W., Machado, N., 1995. Evolução sedimentar do Supergrupo Minas: 500 Ma de registro geológico no Quadrilátero Ferrífero, Minas Gerais, Brasil. Geonomos, 2(1): 1–11.

Ribeiro-Kwitko R., Oliveira, C.G., 2004. O depósito aurífero de Antonio Pereira, Quadrilátero Ferrífero: condições P-T e natureza dos fluidos mineralizadores. Revista Brasileira Geociências 34, 117–126.

Ribeiro-Rodrigues, L.C., de Oliveira, C.G., Friedrich, G., 2007. The Archean BIF-hosted Cuiabá Gold deposit, Quadrilátero Ferrífero, Minas Gerais, Brazil. Ore Geology Reviews 32, 543–570. https://doi.org/10.1016/j.oregeorev.2006.09.001

Rice, C.M., Darke, K.E., Still, J.W., Lachowski, E.E., 1998. Tungsten-bearing rutile from the Kori Kollo gold mine, Bolivia. Mineralogical Magazine 62, 421–429. https://doi.org/10.1180/002646198547684

Richards, J.P., Krogh, T.E., Spooner, E.T.C., 1988. Fluid inclusion characteristics and U–Pb rutile age of late hydrothermal alteration and veining at the Musoshi stratiform copper deposit, Central African copper belt, Zaire. Economic Geology 83, 118–139.

Richards, J.P., Krogh, T.E., Spooner, E.T.C., 1988. Fluid Inclusion Characteristics and U-Pb Rutile Age of Late Hydrothermal Alteration and Veining at the Musoshi Stratiform Copper Deposit, Central African Copper Belt, Zaire. Economic Geology, 83: 118-139.

Roedder, E., 1984. Fluid Inclusions. Reviews in Mineralogy, Vol. 12, Mineralogical Society of America, 644 p.

Roscoe, S.M. 1996. Paleoplacer uranium, gold In O.R. Eckstrand, W.D. Sinclair, and R.I. Thorpe (Eds) Geology of Canadian Mineral Deposits. Geological Survey of Canada, Geology of Canada 8, 10–23.

Scarpelli, W., 1991. Precambrian auriferous quartz-pebble conglomerates in Brazil. Symposium international sur les gisements alluviaux d'or, La Paz, Bolivia, 261–273.

Schieber, J., 2007. Oxidation of detrital pyrite as a cause for Marcasite Formation in marine lag deposits from the Devonian of the eastern US. Deep-sea research. Part II, Topical studies in oceanography 54, 1312–1326. https://doi.org/10.1016/j.dsr2.2007.04.005

Schmitt, A.K., Zack, T., 2012. High-sensitivity U–Pb rutile dating by secondary ion mass spectrometry (SIMS) with an O2+ primary beam. Chemical Geology 332–333, 65-73. https://doi.org/10.1016/j.chemgeo.2012.09.023.

Scott, K.M., 2005. Rutile geochemistry as a guide to porphyry Cu–Au mineralization, Northparkes, New South Wales, Australia. Geochemistry: Exploration, Environment, Analysis 5, 247–253. https://doi.org/10.1144/1467-7873/03-055

Scott, K.M., Radford, N.W., 2007. Rutile compositions at the Big Bell Au deposit as a guide for exploration. Geochemistry: Exploration, Environment, Analysis 7, 353–361. https://doi.org/10.1144/1467-7873/07-135

Scott, K.M., Radford, N.W., Hough, R.M., Reddy, S.M., 2011. Rutile compositions in the Kalgoorlie Goldfields and their implications for exploration. Australian Journal of Earth Sciences 58, 803–812. https://doi.org/10.1080/08120099.2011.600334

Şengün, F., Zack, T., Topuz, G., 2017. Rutile geochemistry and thermometry of eclogites and associated garnet-mica schists in the Biga Peninsula, NW Turkey. Chemie der Erde - Geochemistry 77, 503–515. https://doi.org/10.1016/j.chemer.2017.07.001

Seydoux-Guillaume, A.M., Montel, J.M., Bingen, B., Bosse, V., de Parseval, P., Paquette, J.L., Janots, E., Wirth, R., 2012. Low-temperature alteration of monazite: Fluid mediated coupled dissolution–precipitation, irradiation damage, and disturbance of the U–Pb and Th–Pb chronometers. Chemical Geology 330, 140–158

Seydoux-Guillaume, A.M., Paquette, J.L., Wiedenbeck, M., Montel, J.M., Heinrich, W., 2002. Experimental resetting of the U-Th-Pb systems in monazite. Chemical Geolology 191, 165–181.

Shatsky, V.S., Zedgenizov, D.A., Ragozin, A.L., Kalinina, V. V., 2015. Diamondiferous subcontinental lithospheric mantle of the northeastern Siberian Craton: Evidence from mineral inclusions in alluvial diamonds. Gondwana Research 28, 106–120. https://doi.org/10.1016/j.gr.2014.03.018

Shulaker, D., Schmitt, A., Zack T., Bindeman, I., 2015. In-situ oxygen isotope and trace element geothermometry of rutilated quartz from Alpine fissures. American Mineralogist 100, 915-925. DOI: 10.2138/am-2015-4961.

Silva, A.M., Chemale Jr., F., Heaman, L., 1995. The Ibirité gabbro and the Borrachudo granite - The rift-related magmatism of Mesoproteroic age in the Quadrilátero Ferrífero (MG). Anais VIII Simp. Geol. Minas Gerais, Diamantina, Sociedade Brasileira Geologia/Núcleo MG 13, 89–90.

Smith, S. J., Stevens, R., Liu, S., Li, G., Navrotsky, A., Boerio-Goates, J., Woodfield, B. F., 2009. Heat capacities and thermodynamic functions of TiO2 anatase and rutile: Analysis of phase stability. American Mineralogist 94 (2-3), 236-243.

Spruzeniece, L., Piazolo, S., Daczko, N.R., Kilburn, M.R., Putnis, A., 2017. Symplectite formation in the presence of a reactive fluid: insights from hydrothermal experiments. Journal of Metamorphic Geology 35, 281–299. https://doi.org/10.1111/jmg.12231

Stewart, J., Kerr, G., Prior, D., Halfpenny, A., Pearce, M., Hough, R., Craw, D., 2017. Low temperature recrystallisation of alluvial gold in paleoplacer deposits. Ore Geology Reviews 88, 43–56. https://doi.org/10.1016/j.oregeorev.2017.04.020

Sun, X., Tang, Q., Sun, W., Xu, Li., Zhai, W., Liang, J., Liang, Y., Shen, K., Zhang, Z., Zhou, B., Wang, F., 2007. Monazite, iron oxide and barite exsolutions in apatite aggregates from CCSD drillhole eclogites and their geological implications. Geochimica et Cosmochimica Acta 71 (11), 2896-2905. https://doi.org/10.1016/j.gca.2007.03.030.

Swope, R.J., Smyth, J.R., Larson, A.C., 1995. H in rutile-type compounds; I, Single-crystal neutron and X-ray diffraction study of H in rutile. American Mineralogist 80 (5-6), 448–453. doi: https://doi.org/10.2138/am-1995-5-604

Tanis, E. a., Simon, A., Zhang, Y., Chow, P., Xiao, Y., Hanchar, J.M., Tschauner, O., Shen, G., 2016. Rutile solubility in NaF-NaCl-KCl-bearing aqueous fluids at 0.5-2.79 GPa and 250-650 °C. Geochimica, Cosmochimica Acta 177, 170–181. https://doi.org/10.1016/j.gca.2016.01.003

Taylor, L.A., Keller, R.A., Snyder, G.A., Wang, W., Carlson, W.D., Hauri, E.H., McCandless, T., Kim, K.R., Sobolev, N. V., Bezborodov, S.M., 2000. Diamonds and their mineral inclusions, and what they tell us: A detailed “pull-apart” of a diamondiferous eclogite. International Geology Review 42, 959–983. https://doi.org/10.1080/00206810009465120

Taylor, L.A., Logvinova, A.M., Howarth, G.H., Liu, Y., Peslier, A.H., Rossman, G.R., Guan, Y., Chen, Y., Sobolev, N. V., 2016. Low water contents in diamond mineral inclusions: Proto-genetic origin in a dry cratonic lithosphere. Earth and Planetary Science Letters 433, 125–132. https://doi.org/10.1016/j.epsl.2015.10.042

Teixeira, J.B., Misi, A., Silva, M.G., 2007. Supercontinent evolution and the Proterozoic metallogeny of South America. Gondwana Research 11, 346–361.

Teles, G., Chemale, F., de Oliveira, C.G., 2015. Paleoarchean record of the detrital pyrite-bearing, Jacobina Au-U deposits, Bahia, Brazil. Precambrian Research 256, 289–313. https://doi.org/10.1016/j.precamres.2014.11.004

Tian, W., Chen, B., Ireland, T.R., Green, D.H., Suzuki, K., Chu, Z., 2011. Petrology and geochemistry of dunites, chromitites and mineral inclusions from the Gaositai Alaskan-type complex, North China Craton: Implications for mantle source characteristics. Lithos 127, 165–175.

Trail, D., 2018. Redox-controlled dissolution of monazite in fluids and implications for phase stability in the lithosphere. American Mineralogist 103 (3), 453–461. doi: https://doi.org/10.2138/am-2018-6296

Triebold, S., Luvizotto, G., Tolosana-Delgado, R., Zack, T., Eynatten, H., 2011. Discrimination of TiO2 polymorphs in sedimentary and metamorphic rocks. Contributions to Mineralogy and Petrology 161 (4), 581–596.

Vial, D.S., Abreu, G.C., Schubert, G., Ribeiro-Rodrigues, L.C., 2007a. Smaller gold deposits in the Archean Rio das Velhas greenstone belt, Quadrilátero Ferrífero, Brazil. Ore Geology Reviews 32, 651–673. https://doi.org/10.1016/j.oregeorev.2005.01.004

Vial, D.S., DeWitt, E., Lobato, L.M., Thorman, C.H., 2007b. The geology of the Morro Velho gold deposit in the Archean Rio das Velhas greenstone belt, Quadrilátero Ferrífero, Brazil. Ore Geology Reviews 32, 511–542. https://doi.org/10.1016/j.oregeorev.2004.12.008

Vial, D.S., Duarte, B.P., Fuzikawa, K., Vieira, M.B.H., 2007c. An epigenetic origin for the Passagem de Mariana gold deposit, Quadrilátero Ferrífero, Minas Gerais, Brazil. Ore Geology Reviews 32, 596–613. https://doi.org/10.1016/j.oregeorev.2005.03.017

Vial, D.S., Ferreira Jr., M.G., Ferrari, P.G., 1987. A lapa seca na mina de Morro Velho: metavulcanitos alterados hidrotermalmente. Sociedade Brasileira de Geologia, Simpósio de Geologia de Minas Gerais, 4. Belo Horizonte. Anais 7, pp. 369–390.

Vial, D.S., Groves, D.I., Cook, N.J., Lobato, L.M., 2007d. Special issue on gold deposits of Quadrilátero Ferrífero, Minas Gerais, Brazil. Ore Geology Reviews 32, 469–470. https://doi.org/10.1016/j.oregeorev.2006.11.006

Villaça, J.N., 1981. Alguns aspectos sedimentares da Formação Moeda. Sociedade Brasileira Geologia, Núcleo MG 2, 92-137.

Villaça, J.N., Moura, L.A.M., 1981. Uranium in Precambrian Moeda Formation, Minas Gerais, Brazil: U.S. Geological Survey Professional Paper 1161, p. 1-14.

Wallace, R.M., 1958. The Moeda Formation. Symposium on the stratigraphy of the Minas series in the Quadriláterro Ferrífero, Minas Gerais, Brazil. Boletim da Sociedade Brasileira de Geologia 7 (2), 59-60.

Wedepohl, K.H., 1991. Chemical composition and fractionation of the continental crust. Geologische Rundschau 80, 225-231.

Whymark, W.E., Frimmel, H.E., 2017. Regional gold-enrichment of conglomerates in Paleoproterozoic supergroups formed during the 2.45Ga rifting of Kenorland. Ore Geology Reviews https://doi.org/10.1016/j.oregeorev.2017.04.003

Wilkinson, J., 2001. Fluid inclusions in hydrothermal ore deposits. Lithos 55, 229–272. https://doi.org/10.1016/S0024-4937(00)00047-5

Williams S.A. Cesbron F.P., 1977. Rutile and apatite: Useful prospecting guides for porphyry copper deposits: Mineralogical Magazine 41, 288–292.

Wilson, S.A., 1997, The collection, preparation, and testing of USGS reference material BCR-2, Columbia River, Basalt: U.S. Geological Survey Open-File Report 98.

Xiaoming Sun, Tang, Q., Sun, W., Xu, L., Zhai, W., Liang, J., Liang, Y., Shen, K., Zhang, Z., Zhou, B., Wang, F., 2007. Monazite, iron oxide and barite exsolutions in apatite aggregates from CCSD drillhole eclogites and their geological implications>. Geochimica et Cosmochimica Acta 71, 2896–2905. https://doi.org/10.1016/j.gca.2007.03.030

Yamamoto, S., Komiya, T., Hirose, K., Maruyama S., 2009. Coesite and clinopyroxene exsolution lamellae in chromites: In-situ ultrahigh-pressure evidence from podiform chromitites in the Luobusa ophiolite, southern Tibet. Lithos 109, 314-322.

Ye, K., Yao, Y., Katayama, I., Cong, B., Wang, Q., Maruyama, S., 2000. Large areal extent of ultrahigh-pressure metamorphism in the Sulu ultrahigh-pressure terrane of East China: new implications from coesite and omphacite inclusions in zircon of granitic gneiss. Lithos 52, 157–164.

Zack T., Kooijman E., 2017. Petrology and geochronology of rutile. Reviews in Mineralogy and Geochemistry 83, 443–467.

Zack, T., Kronz, A., Foley, S.F., Rivers, T., 2002. Trace element abundances in rutiles from eclogites and associated garnet mica schists. Chemical Geology 184, 97–122. https://doi.org/10.1016/S0009-2541(01)00357-6

Zack, T., Moraes, R., Kronz, A., 2004. Temperature dependence of Zr in rutile: empirical calibration of a rutile thermometer. Contributions to Mineralogy and Petrology 148, 471–488. https://doi.org/10.1007/s00410-004-0617-8

Zack, T., Stockli, D.F., Luvizotto, G.L., Barth, M.G., Belousova, E., Wolfe, M.R., Hinton, R.W., 2011. In situ U-Pb rutile dating by LA-ICP-MS:208Pb correction and prospects for geological applications. Contributions to Mineralogy and Petrology 162, 515–530. https://doi.org/10.1007/s00410-011-0609-4

Zeh, A., Cabral, A.R., Koglin, N., Decker, M., 2018. Rutile alteration and authigenic growth in metasandstones of the Moeda Formation, Minas Gerais, Brazil – A result of Transamazonian fluid–rock interaction. Chemical Geology 483, 397-409. https://doi.org/10.1016/j.chemgeo.2018.03.007

Figure 1 – preferred size 30/40mm (Small size)

Figure 1. Schematic diagram of prismatic and basal section of rutile. In the prismatic section, both cleavage and geniculated twin are illustrated at {101} and {301}, respectively, and oscillatory zoning illustrated in the basal section. Different types of mineral inclusions are illustrated, A- protogenetic, B- syngenetic, C-epigenetic or secondary, D-dissolution and precipitation related to highly porous domains.

Figure 2 – preferred size 140mm (1.5 column)

Figure 2. Simplified geological map of the QF, Brazil. Modified after Scarpelli (1991); Alkmim and Marshak (1998); Ribeiro-Kwitko and Oliveira (2004); Baltazar and Zuchetti (2007), Vial et al. (2007a) and Koglin et al. (2012). Sampling – (dark) purple circles - correspond to: *A. 4517, B. 4524, C. AA01, D. 4518, E. 4522, and F.4520.*

Figure 3 – preferred size 190mm (double column)

Figure 3. SEM micrographs of sample AA01 in BSE showing: I and II. rutile spatially associated with coarse quartz or disseminated within quartz grains, surrounded by very fine-grained matrix; III and IV. Rutile grains found within the foliated matrix associated with gold; V. rutile grains showing pervasive secondary inclusions of matrix minerals; VI. Grains showing dissolution front (dashed line and arrow) and primary zircon inclusions; VII. grains exhibiting very porous textures with pyrrhotite and Fe oxides associated to the pores; VIII. Small pyrite inclusions and pervasive matrix secondary inclusions; and IX. Presence of xenotime as a secondary alteration product of zircon.

Figure 4 – preferred size 90mm (single column)

Figure 4. Combined histogram of the recurrence of representative mineral inclusions in the bulk of mineral inclusions for each sample. Ngrtotal=371 grains: n4524=30; n4517=75; n4520=52; n4522=70; n4518=144. Ninctotal=947 inclusions. Average inclusion/grain ratio of 2.5 (max 3.1 and min 2.0). *variation of the type of oxide is possible.

Figure 5 – preferred size 190mm (double column)

Figure 5. SEM-BSE micrographs of sample A. 4517 and B. 4524 showing: A-I. Monazite intergrowths and patchy zoning; A-II. Monazite and scheelite primary inclusions; A-III. Primary uranium-oxide inclusions (tentatively ascribed to uraninite); A-IV. Pervasive silicate secondary inclusions, with grains showing patchy zoning and a primary chalcopyrite inclusion; A-V. Zircon inclusions; A-VI. Scheelite primary inclusions and Th-oxide mineral (tentatively ascribed to thorite); B-I. primary chalcocite inclusion and needle-shape secondary inclusions; B-II. Primary uraninite inclusions; B-III. Development of porosity and patchy zoning; B-IV. Secondary oxidation of primary inclusions; B-V. rutile with a mottled arrangement of uranium-bearing oxide and having a highly porous texture; and B-VI. Micron-size monazite inclusions and bright BSE twins, highlighting preferential crystallographic trace element intake in rutile (arrows).

Figure 6 – preferred size 190mm (double column)

Figure 6. SEM micrographs of sample 4518 in BSE showing: I. patchy zoning (arrow) and primary bethierite, tetrahedrite and arsenopyrite inclusions; II. Primary monazite, arsenopyrite and pyrrhotite inclusions; III. Highly porous texture, with silicate inclusions; IV. Secondary silicate inclusions, cross-cutting rutile, with primary tetrahedrite inclusions; V. primary stibnite, tetrahedrite and micron-sized arsenopyrite inclusions and patchy zoning (arrow); VI. Elongated shape with pyrite inclusions; VII. rare tennantite primary inclusion in a porous rutile grain; VIII. Secondary alteration xenotime in a highly porous grain, infilled with silicate minerals; IX. Primary zircon inclusion and rutile with patchy zoning (arrow); X. rare plagionite, associated with arsenopyrite and pyrrhotite; and XI. Secondary alteration of rutile with fractures and pores infilled with white mica and quartz.

Figure 7 – preferred size 190mm (double column)

Figure 7. SEM-BSE micrographs of sample A. 4522 and B. 4520 showing: A-I. Cr-oxide inclusions (tentatively ascribed to chromite) spatially arranged in a circle, as the contour of the grain – potentially an exsolution feature; A-II. Primary arsenopyrite inclusions intergrowing with rutile; A-III. Zircon and monazite occur as mineral intergrowths in quite altered rutile grains; A-IV. Oxidation of primary inclusions within rutile, associated with needle-shaped silicate secondary inclusions; B-I. a preserved pyrrhotite primary inclusion; B-II. Pyrite and silicate inclusions; B-III. Primary tetrahedrite inclusion in a slightly zoned rutile; B-IV. Less porous grain with pyrrhotite; and B-V. a primary zircon inclusion.

Figure 8 – preferred size 140mm (1.5 column)

Figure 8. Cr-Nb discrimination diagram for rutile after Zack et al. (2004) and later modified by Meinhold et al. (2008). Symbols correspond to rutiles from different samples; n=275. Note the very high Nb-enrichment in rutiles from sample 4517.

Figure 9 – preferred size 90mm (single column)

Figure 9. Ternary diagram for rutile compositions in mesothermal gold deposits after Clarke and Williams-Jones (2004) typifying areas of barren, sub-ore alteration and ore zone type rutile. Symbols correspond to rutiles from different samples; n=107 out of 275.

Figure 10 – preferred size 90mm (single column)

Figure 10. Ternary diagrams of rutile compositions highlighting sourcing and different mineral chemistry of grains within the Moeda Formation, SSFC. a) Ti-Nb+Fe-Cr; b) Cr-Fe-Nb; c) Nb+Fe-W-Cr; and d) Fe-Nb(Cr)-V diagrams. Symbols correspond to different samples, and box with cross to rutiles with high-W concentrations (proximal to Au). Average rutile compositions were determined combining metamorphic rutile data from the literature (see section 4.2.2). Abbreviations: BIF - Banded Iron Formation.

Figure 11 – preferred size 90mm (single column)

Figure 11. Zr/Hf vs Nb/Ta diagram for rutiles of different rock types, such as peridotites (mantle), different metamorphic-grade rocks and rutiles precipitated from fluids/post-depositional (hydrothermal). Data was compiled from 1. Kalfoun et al. (2002), 2. Lorand and Gregoire (2010), 3. Şengün et al. (2017), 4. Zack et al. (2002), 5. Hart et al. (2016), 6.John et al. (2011), 7. Zeh et al. (2018) and this study. Light-coloured diamond symbols correspond to W-rich, U-Pb dated detrital grains (orogenic gold related), and W-rich, with no concordant U-Pb data (W-rich). Note how rutiles with an orogenic gold signature plot within the field of metamorphic rutile, and authigenic, fluid-related rutiles plot separately.

Figure 12 – preferred size 60mm (small size)

Figure 12. Principal components 1 and 2 from PCA using GCDKit (Janousek et al., 2006; 2011) for a) dataset excluding Ti; b) dataset including Ti. n=43. Black arrows highlight the eigenvectors and their comparable weight for PC1 and/or PC2. Different symbols correspond to different samples. Ti, Nb, Fe, and Cr are the main chemical vectors, while W has a smaller but still statistically representative weight in PC2.

Figure 13 – preferred size 90mm (single column)

Figure 13. Rutile Wetherill Concordia diagram and $^{207}Pb/^{206}Pb$ probability density plot for metaconglomerate AA01, from Unit I. All reported uncertainties are 2-sigma. Grain age is given based on the $^{207}Pb/^{206}Pb$ ratio. The rutile grain shown corresponds to one of the Pb_{cm}-free grains exhibiting a dissolution front and zircon micro-inclusions.

Figure 14 – preferred size 140mm (1.5 column)

Figure 14. Rutile U-Pb Wetherill Concordia diagrams for: a) sample 4517; b) sample 4524; c) sample 4522; d) sample 4518. Discordia lines were chosen based on the U-Pb associations between the detrital populations. All reported uncertainties are 2-sigma. Grain ages are given based on the $^{207}Pb/^{206}Pb$ ratio. Faded grey circles represent data points not included in the upper intercept determination ages.

Figure 15 – preferred size 90mm (single column)

Figure 15. Frequency histograms for $^{207}Pb/^{206}Pb$ detrital ages of zircon and rutile from the Moeda Formation. a) sample 4517; b) sample 4520 combined with sample 4522; c) sample 4518. Zircon data from Martinez-Dopico et al. (2017). Relative probability density curves were not included due to the large propagated uncertainties associated with Pb_{cm} corrections on the $^{207}Pb/^{206}Pb$ ages. SB – Sabará; RVI – Rio das velhas I; RVII – Rio das Velhas II; MI – Mamona I; MII – Mamona II events.

Figure 16 – preferred size 90mm (single column)

Figure 16. Wetherill Concordia diagram showing two different sets of U-Pb modelled mixing examples; (A) between 2.1 and 2.66 Ga; (B) between 2.0 and 2.72 Ga. Error ellipses are 2-sigma. Darker circle corresponds to inherited component, while lighter circle corresponds to newly formed component, and colour-shades in between correspond to given proportions noted in grey as a ratio.

Figure 17 – preferred size 90 or 140mm (single or 1.5 column)

Figure 17. 3-D block diagrams representing the sequence of events in the Quadrilátero Ferrífero, SSFC, emphasising the gold precipitation and remobilisation stages, including detailed graphical zooms. A) Gold precipitation during the late Archean, with co-precipitation of sulphides and rutile; b) Early Paleoproterozoic intracratonic rifting and deposition of the gold-bearing horizons of the Moeda Formation, including detrital pyrite, gold and rutile; c) later tectonometamorphic events (Paleoproterozoic and/or Neoproterozoic in age) that affect the SSFC, generating a large-scale fluid circulation that is responsible for the gold remobilisation by dissolution and reprecipitation. Rutile testifies a stage of dissolution, partial Pb-loss and new growth during these events. For the gold dissolution, remobilisation, and co-precipitation again with tourmaline it is suggested a boron-rich fluid composition with complex chemistry.

Table 1. Principal component analysis (PCA) results summary, including eigenvalues, and factor loadings determination using covariance of n=43 population. Parameters used include Nb, Ta, W, Fe, V, Cr and Sb, with and without Ti.

Table 1

PCA including Ti

	Comp.1	Comp.2	Comp.3	Comp.4	Comp.5	Comp.6	Comp.7	Comp.8
Eigenvalue	9857.289	3794.184	1972.85	1599.092	870.4408	247.5438	63.18771	24.46331
Variability	0.817658	0.121142	0.032753	0.021518	0.006376	0.000516	3.36E-05	5.04E-06
Cumulative proportion	0.817658	0.938799	0.971552	0.99307	0.999446	0.999961	0.99999	1
Factor Loadings	Comp.1	Comp.2	Comp.3	Comp.4	Comp.5	Comp.6	Comp.7	Comp.8
Nb	-0.494	0.543	0.383	-0.405	-0.385			
Ta						0.995		
W			-0.776	-0.628				
Fe	-0.279	0.52	-0.144	0.16	0.774			
V							0.994	
Cr	-0.393	0.459	-0.623	0.491				
Sb								0.999
Ti	0.821	0.528	0.14	-0.164				

PCA excluding Ti

	Comp.1	Comp.2	Comp.3	Comp.4	Comp.5	Comp.6	Comp.7
Eigenvalue	6366.692	2171.897	1746.235	870.4607	247.9151	63.80517	24.71326
Variability	0.825134	0.096023	0.062073	0.015424	0.001251	8.29E-05	1.24E-05
Cumulative proportion	0.825134	0.921157	0.98323	0.998654	0.999905	0.999988	1
Factor Loadings	Comp.1	Comp.2	Comp.3	Comp.4	Comp.5	Comp.6	Comp.7
Nb	0.835	0.362	-0.135	0.386			
Ta					-0.995		
W		-0.44	-0.896				
Fe	0.522	-0.322	0.135	-0.774			
V						-0.995	
Cr	-0.164	0.756	-0.4	-0.49			
Sb							0.999

RESEARCH HIGHLIGHTS

- MULTIPLE STAGES OF FLUID-INDUCED GOLD REMOBILISATION IN PALEOPROTEROZOIC PLACER
- MINERAL INCLUSIONS IN RUTILE CAN BE USED AS AN EFFECTIVE PROVENANCE TOOL
- NB/TA VS ZR/HF VALUES DISCRIMINATE DIFFERENT TYPES OF RUTILE

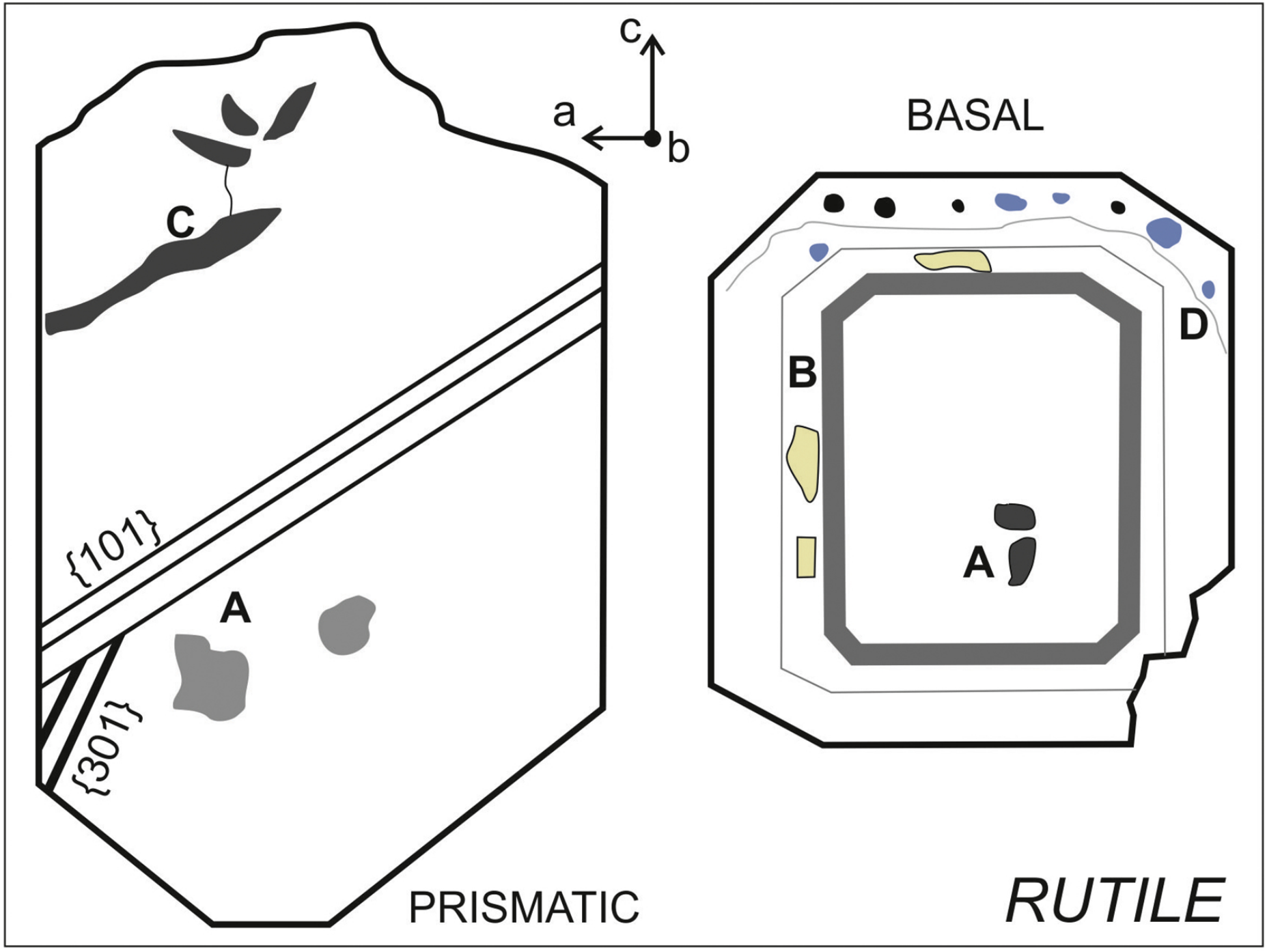

Figure 1

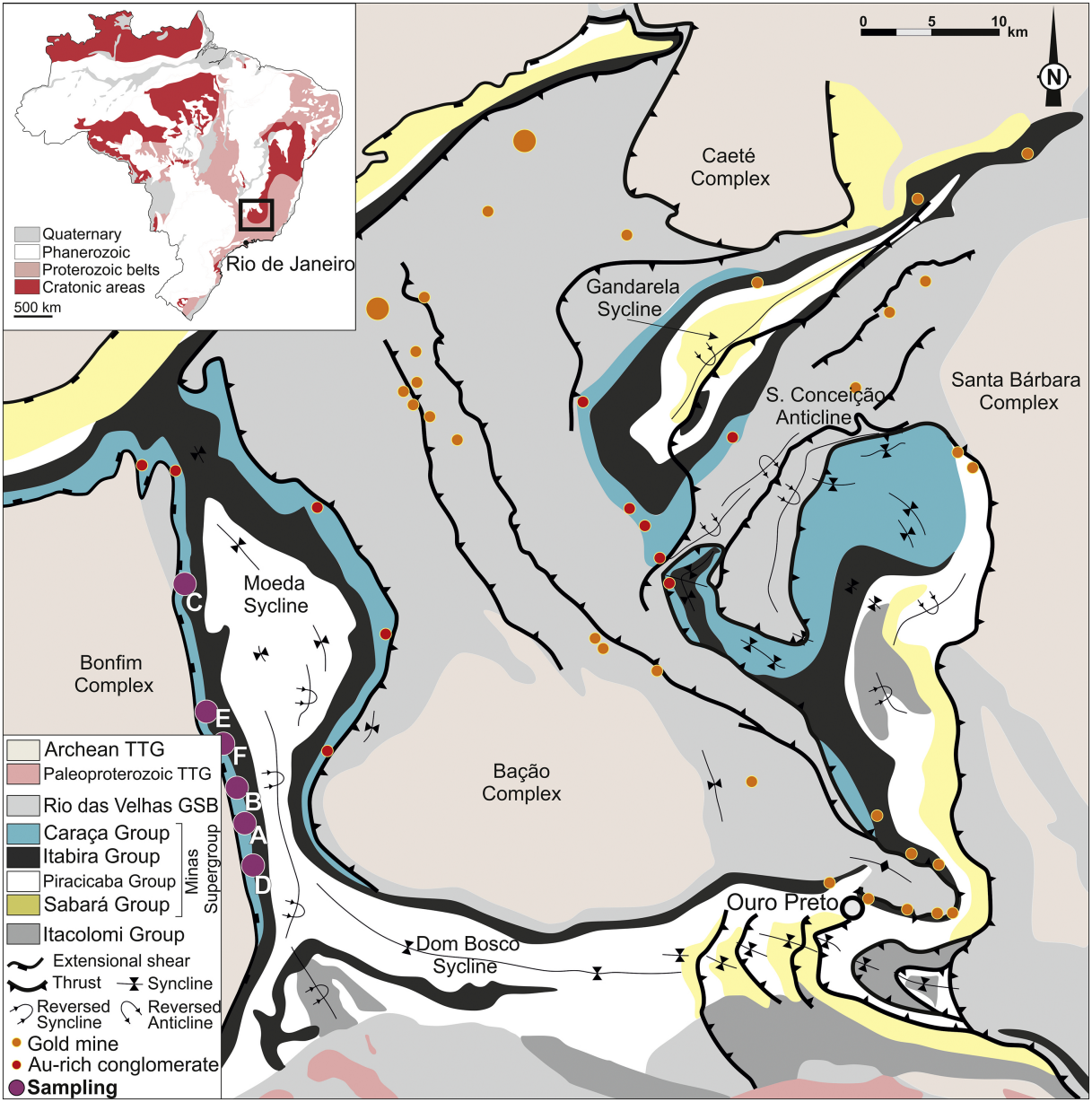
Quaternary
Phanerozoic
Proterozoic belts
Cratonic areas
500 km
Rio de Janeiro
0
5
10
km
N
Caeté
Complex
Gandarela
Sycline
S. Conceição
Anticline
Santa Bárbara
Complex
Moeda
Sycline
Bonfim
Complex
Bação
Complex
Dom Bosco
Sycline
Ouro Preto
C
E
F
B
A
D
Archean TTG
Paleoproterozoic TTG
Rio das Velhas GSB
Caraça Group
Itabira Group
Piracicaba Group
Sabará Group
Minas
Supergroup
Itacolomi Group
Extensional shear
Thrust
Syncline
Reversed
Syncline
Reversed
Anticline
Gold mine
Au-rich conglomerate
Sampling

Figure 2

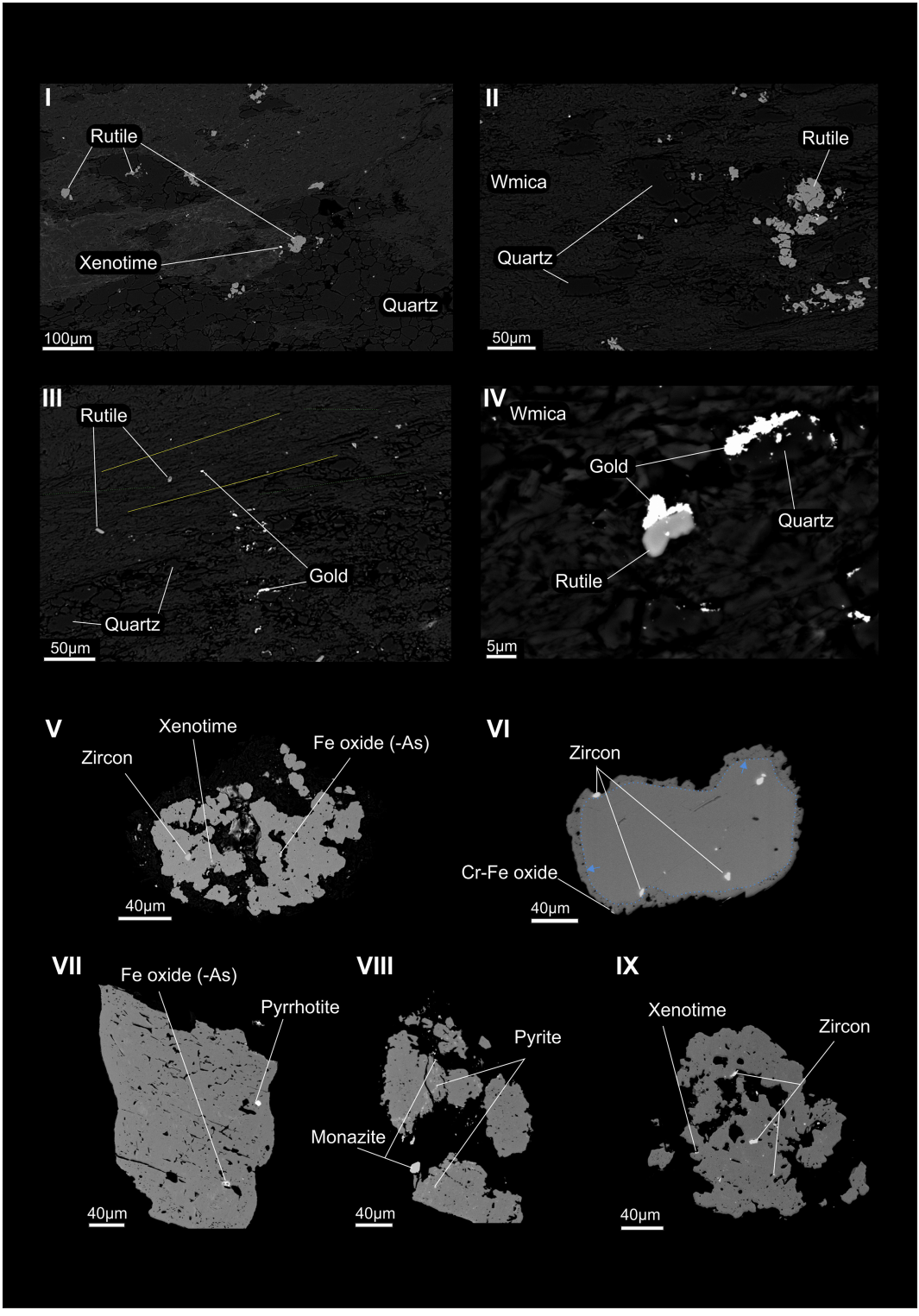
I
Rutile
Xenotime
Quartz
100µm
II
Rutile
Wmica
Quartz
50µm
III
Rutile
Gold
Quartz
50µm
IV
Wmica
Gold
Quartz
Rutile
5µm
V
Xenotime
Zircon
Fe oxide (-As)
40µm
VI
Zircon
Cr-Fe oxide
40µm
VII
Fe oxide (-As)
Pyrrhotite
40µm
VIII
Pyrite
Monazite
40µm
IX
Xenotime
Zircon
40µm

Figure 3

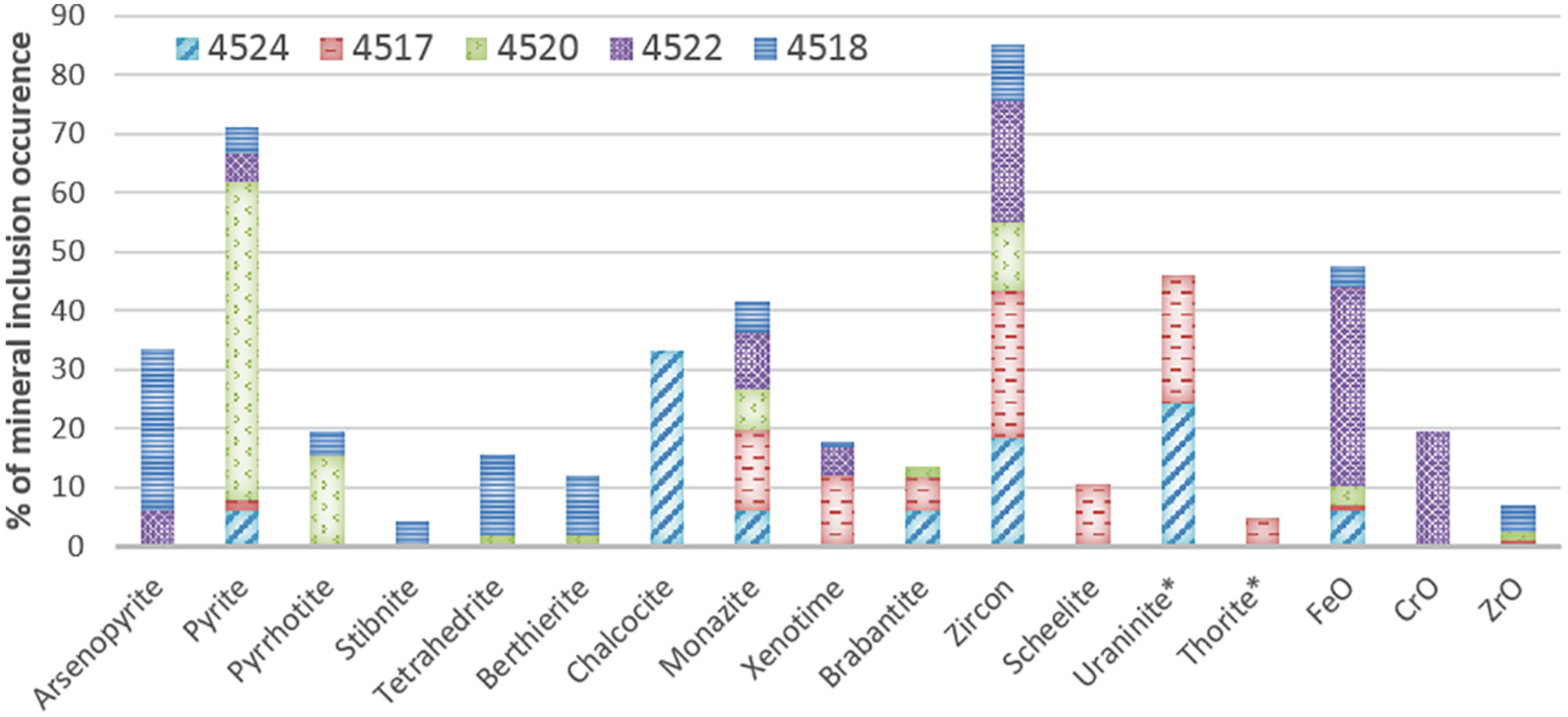
% of mineral inclusion occurence
90
80
70
60
50
40
30
20
10
0
4524
4517
4520
4522
4518
Arsenopyrite
Pyrite
Pyrrhotite
Stibnite
Tetrahedrite
Berthierite
Chalcocite
Monazite
Xenotime
Brabantite
Zircon
Scheelite
Uraninite*
Thorite*
FeO
CrO
ZrO

Figure 4

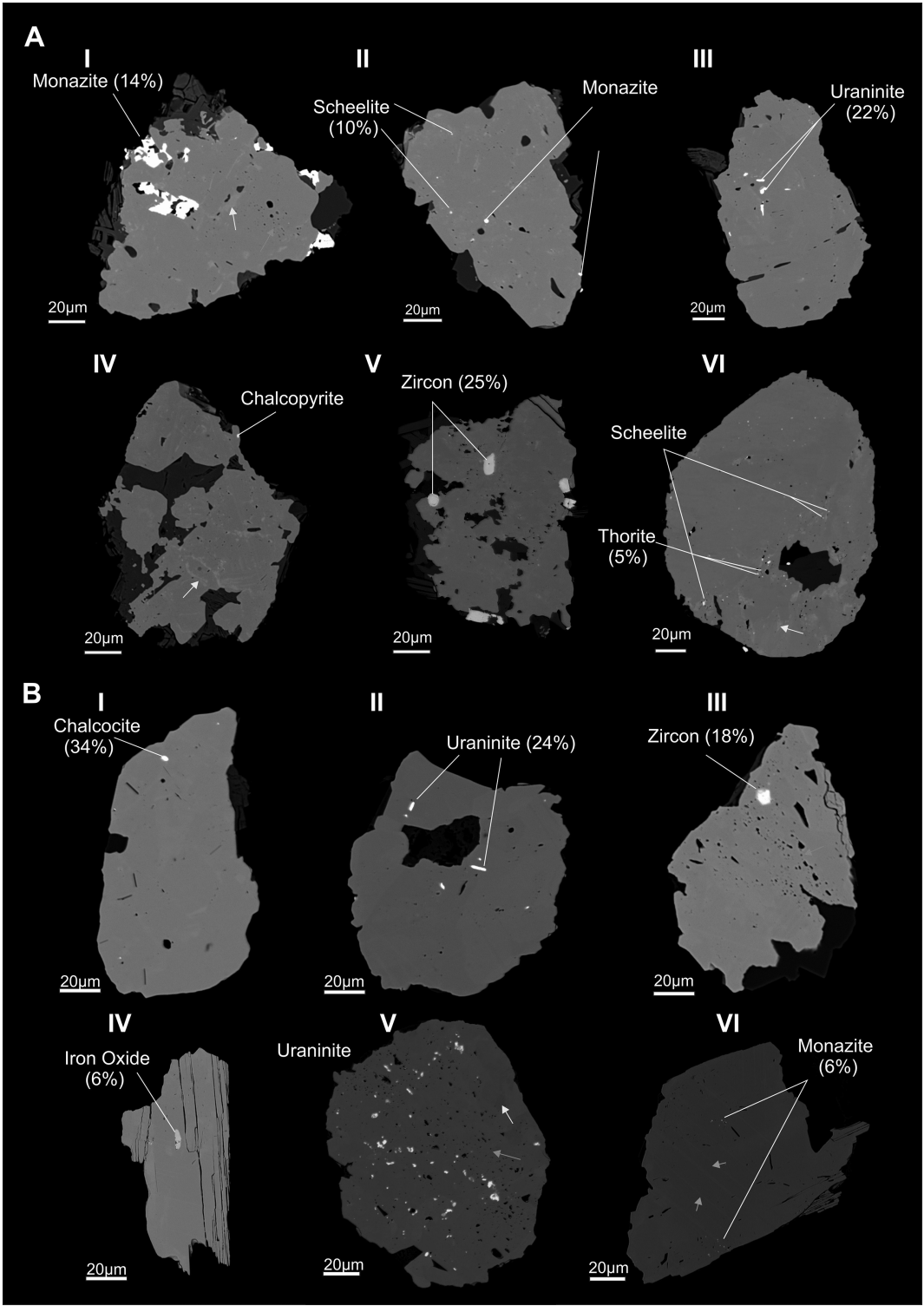
A
I
Monazite (14%)
20μm
II
Scheelite
(10%)
Monazite
20μm
III
Uraninite
(22%)
20μm
IV
Chalcopyrite
20μm
V
Zircon (25%)
20μm
VI
Scheelite
Thorite
(5%)
20μm
B
I
Chalcocite
(34%)
20μm
II
Uraninite (24%)
20μm
III
Zircon (18%)
20μm
IV
Iron Oxide
(6%)
20μm
V
Uraninite
20μm
VI
Monazite
(6%)
20μm

Figure 5

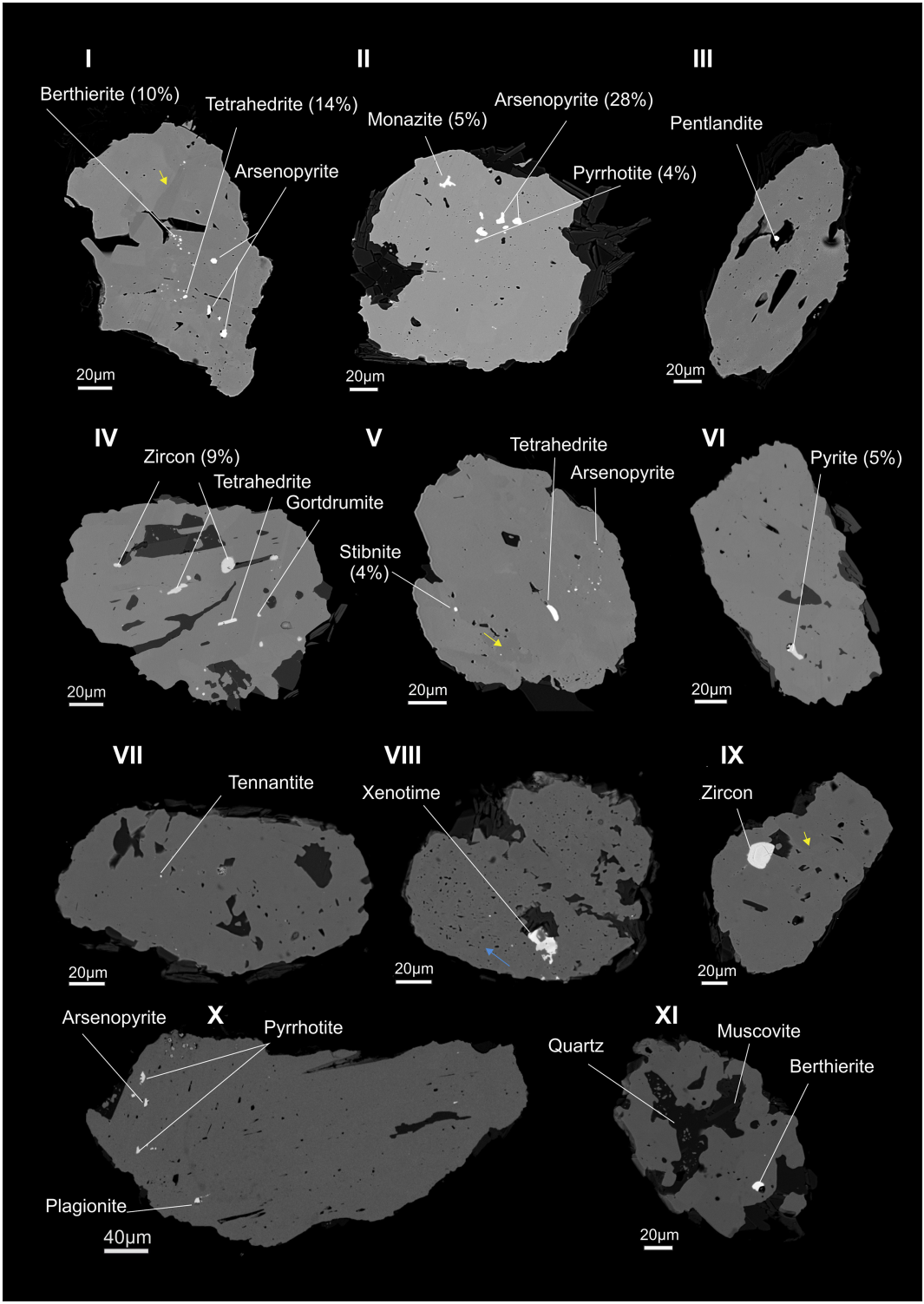
I
Berthierite (10%)
Tetrahedrite (14%)
Arsenopyrite
20μm
II
Monazite (5%)
Arsenopyrite (28%)
Pyrrhotite (4%)
20μm
III
Pentlandite
20μm
IV
Zircon (9%)
Tetrahedrite
Gortdrumite
20μm
V
Stibnite (4%)
Tetrahedrite
Arsenopyrite
20μm
VI
Pyrite (5%)
20μm
VII
Tennantite
20μm
VIII
Xenotime
20μm
IX
Zircon
20μm
X
Arsenopyrite
Pyrrhotite
Plagionite
40μm
XI
Quartz
Muscovite
Berthierite
20μm

Figure 6

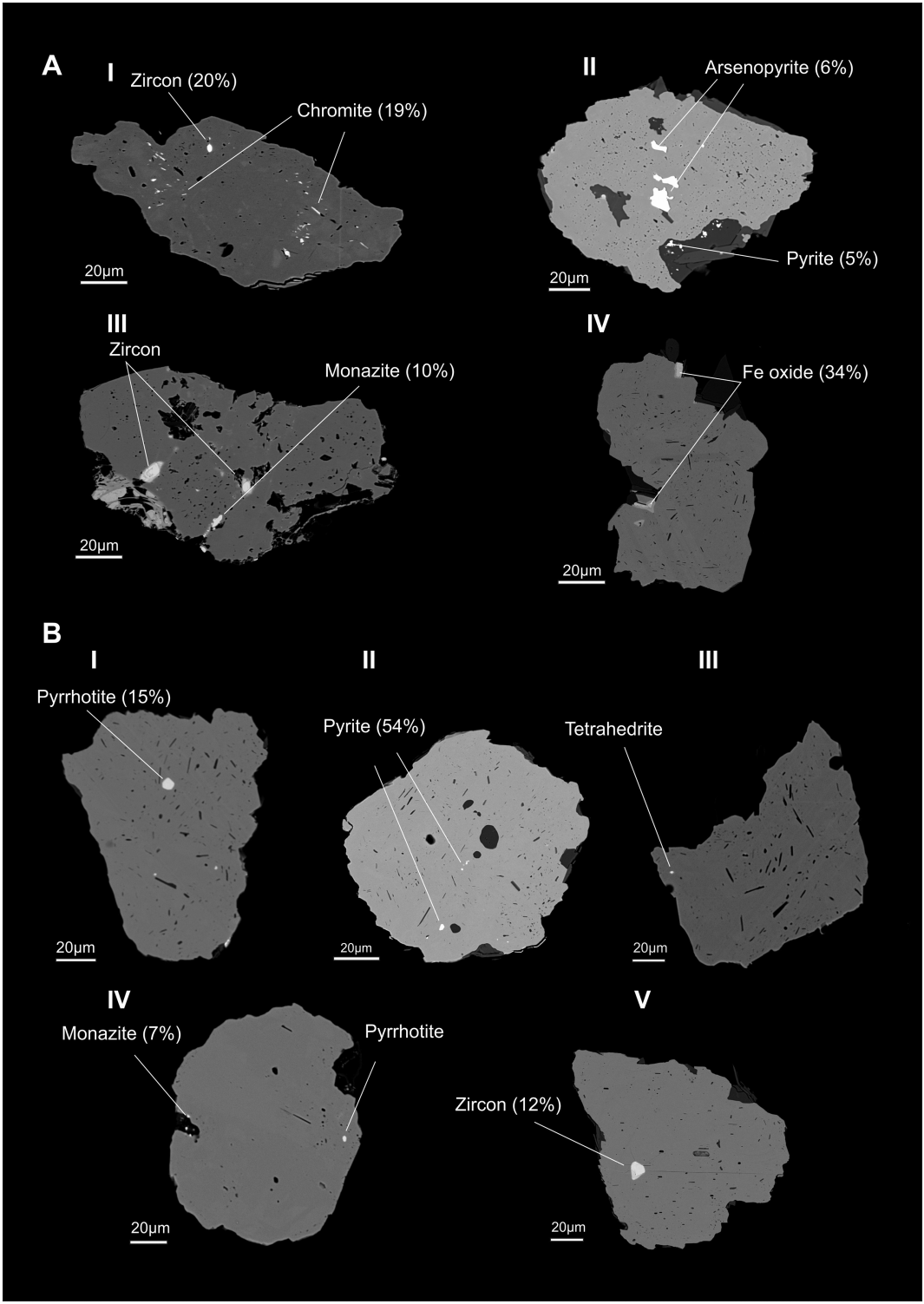
A
I
Zircon (20%)
Chromite (19%)
20μm
II
Arsenopyrite (6%)
Pyrite (5%)
20μm
III
Zircon
Monazite (10%)
20μm
IV
Fe oxide (34%)
20μm
B
I
Pyrrhotite (15%)
20μm
II
Pyrite (54%)
20μm
III
Tetrahedrite
20μm
IV
Monazite (7%)
Pyrrhotite
20μm
V
Zircon (12%)
20μm

Figure 7

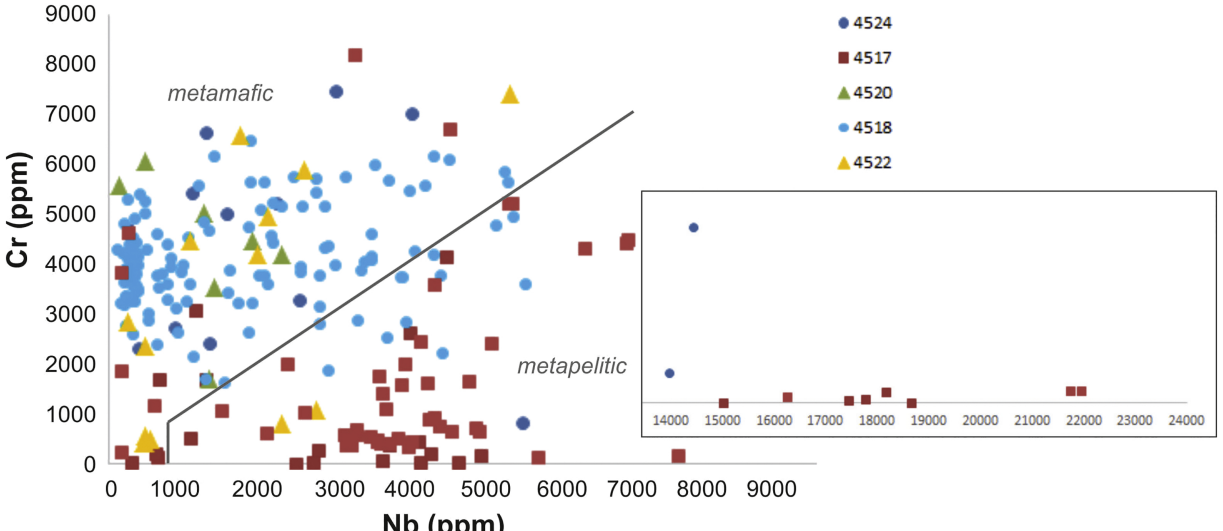
Cr (ppm)
Nb (ppm)
metamafic
metapelitic
4524
4517
4520
4518
4522
0
1000
2000
3000
4000
5000
6000
7000
8000
9000
14000
15000
16000
17000
18000
19000
20000
21000
22000
23000
24000

Figure 8

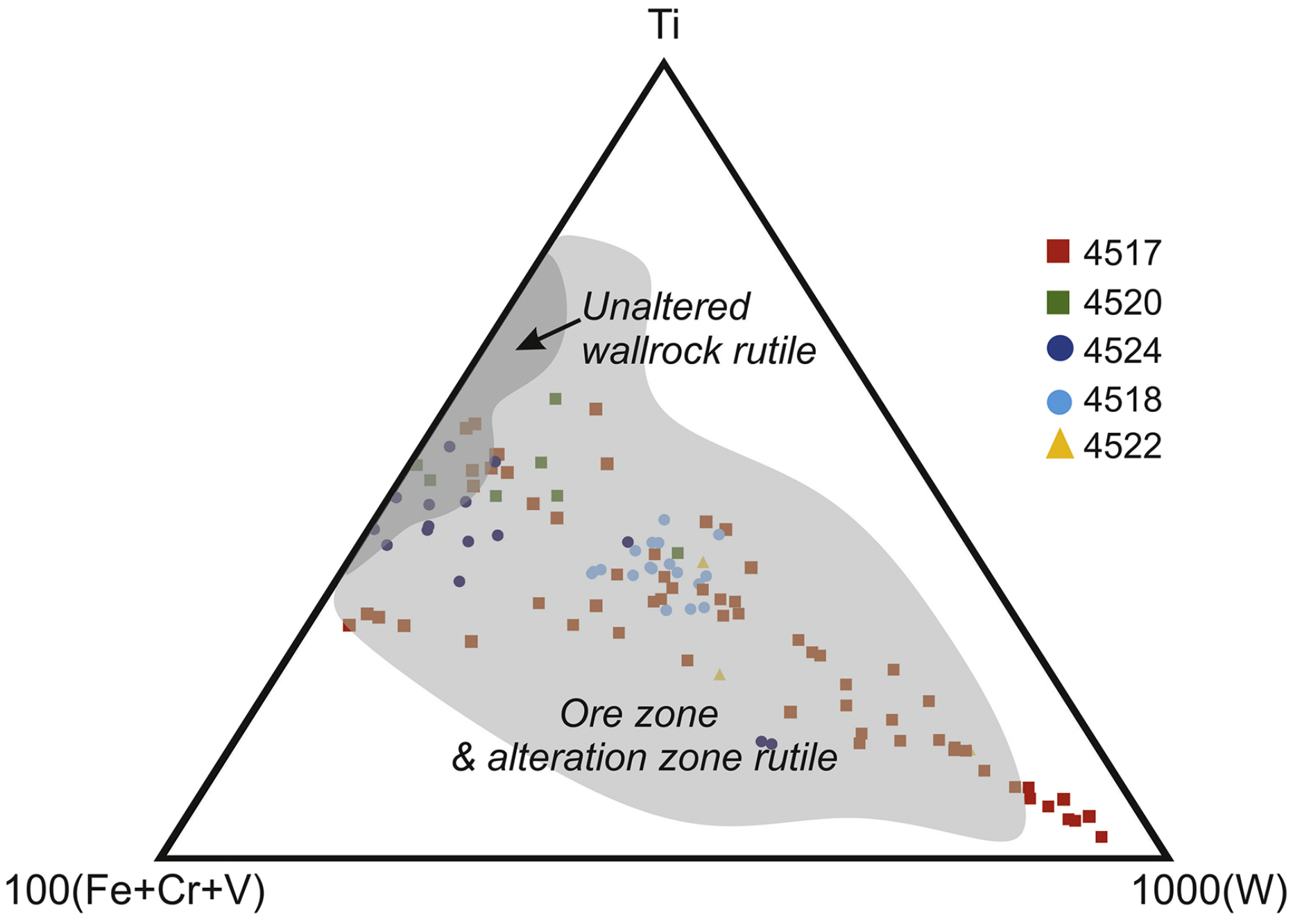
Ti
100(Fe+Cr+V)
1000(W)
Unaltered
wallrock rutile
Ore zone
& alteration zone rutile
4517
4520
4524
4518
4522

Figure 9

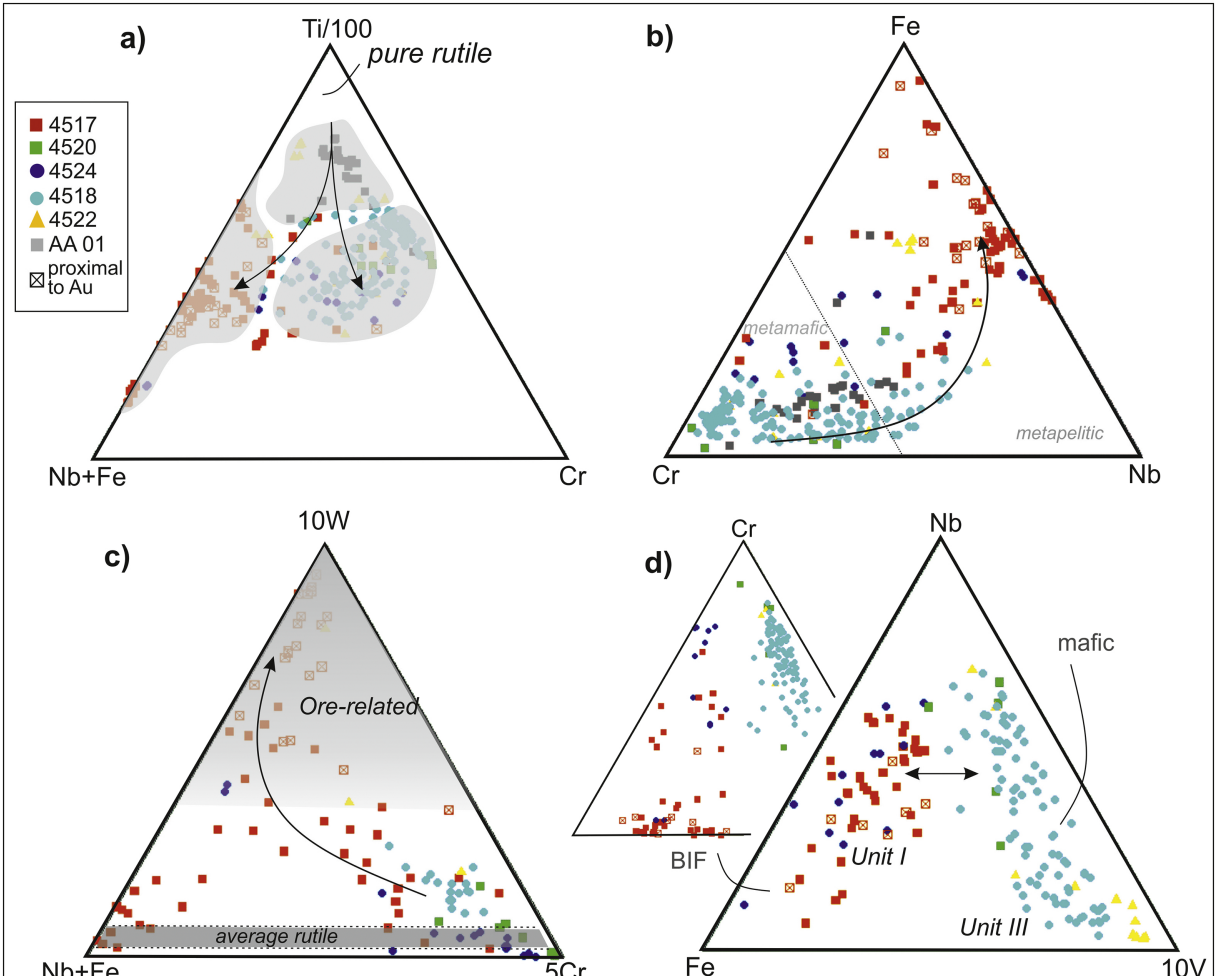
a)
Ti/100
pure rutile
4517
4520
4524
4518
4522
AA 01
proximal to Au
Nb+Fe
Cr
b)
Fe
metamafic
metapelitic
Cr
Nb
c)
10W
Ore-related
average rutile
Nb+Fe
5Cr
d)
Cr
Nb
mafic
BIF
Unit I
Unit III
Fe
10V

Figure 10

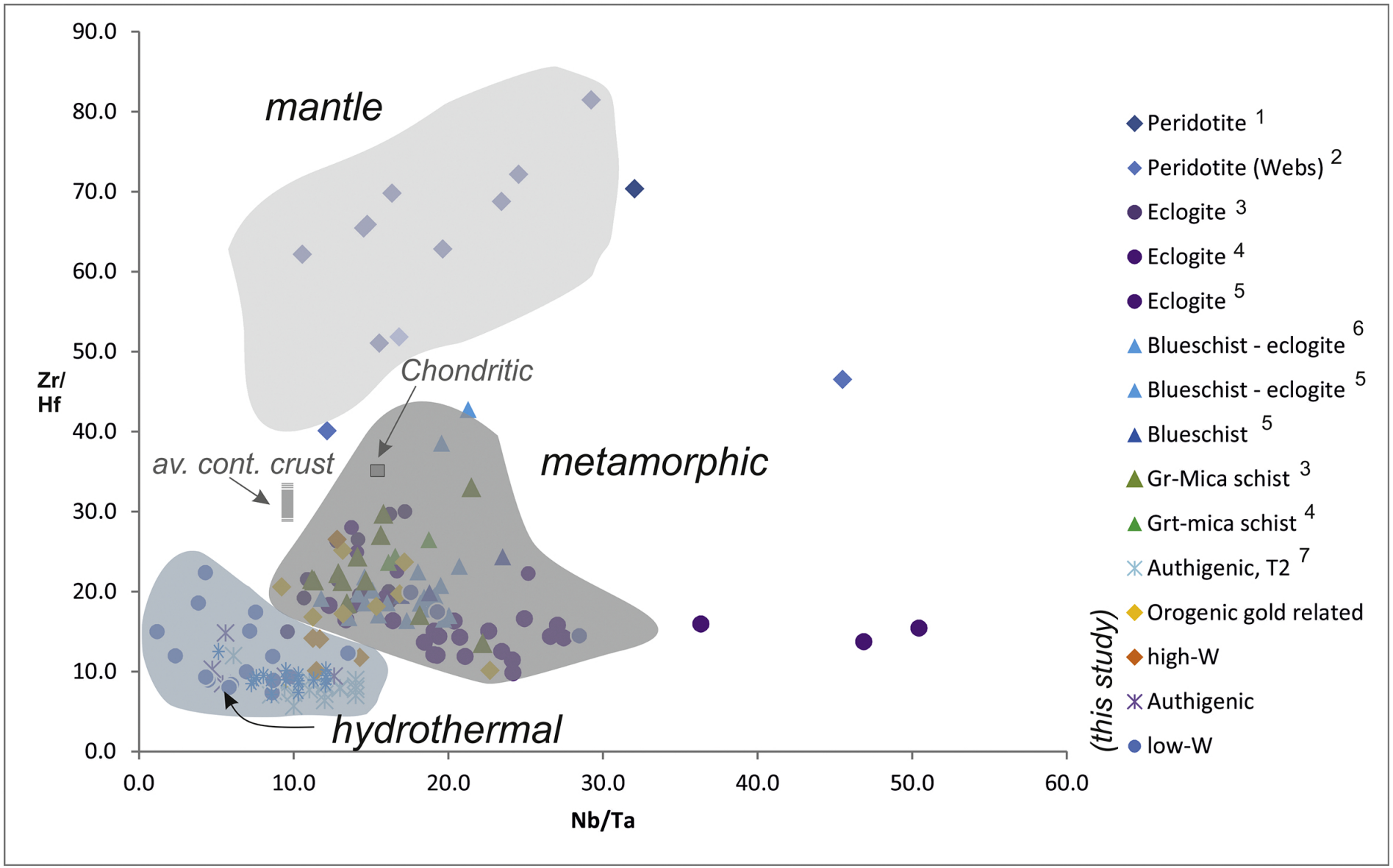
mantle
Chondritic
av. cont. crust
metamorphic
hydrothermal
Zr/Hf
Nb/Ta
0.0
10.0
20.0
30.0
40.0
50.0
60.0
70.0
80.0
90.0
Peridotite 1
Peridotite (Webs) 2
Eclogite 3
Eclogite 4
Eclogite 5
Blueschist - eclogite 6
Blueschist - eclogite 5
Blueschist 5
Gr-Mica schist 3
Grt-mica schist 4
Authigenic, T2 7
Orogenic gold related
high-W
Authigenic
low-W
(this study)

Figure 11

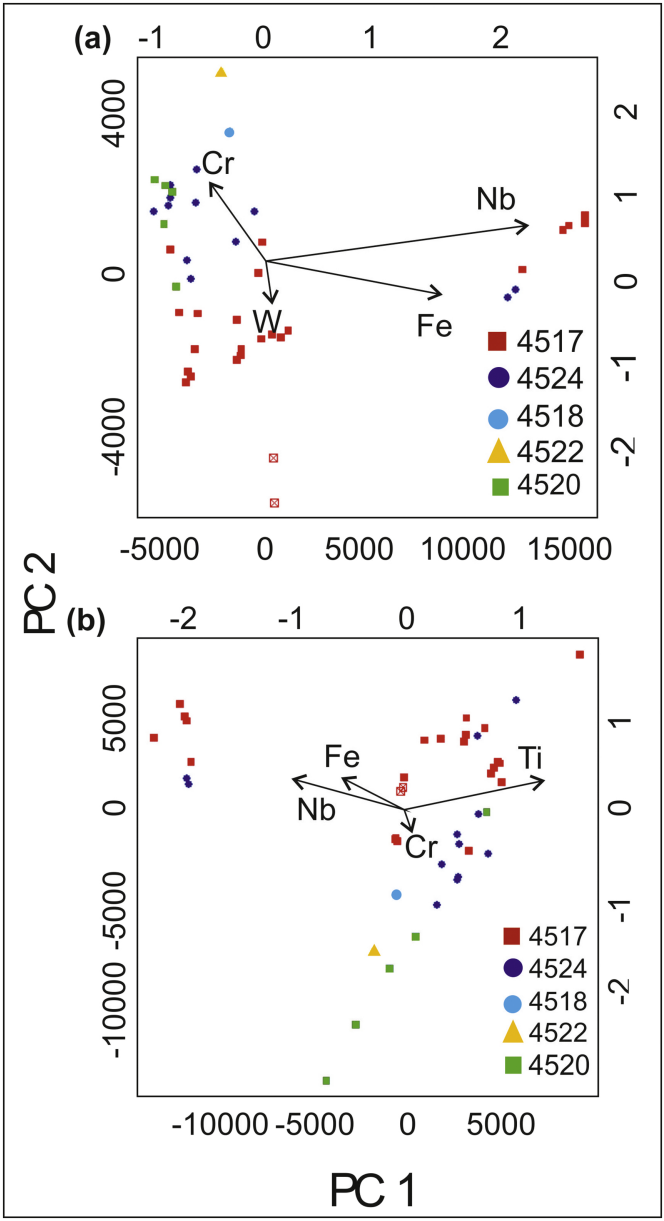
(a)
-1
0
1
2
4000
0
-4000
Cr
Nb
W
Fe
4517
4524
4518
4522
4520
2
1
0
-1
-2
-5000
0
5000
10000
15000
PC 2
(b)
-2
-1
0
1
5000
0
-5000
-10000
Fe
Ti
Nb
Cr
4517
4524
4518
4522
4520
1
0
-1
-2
-10000
-5000
0
5000
PC 1

Figure 12

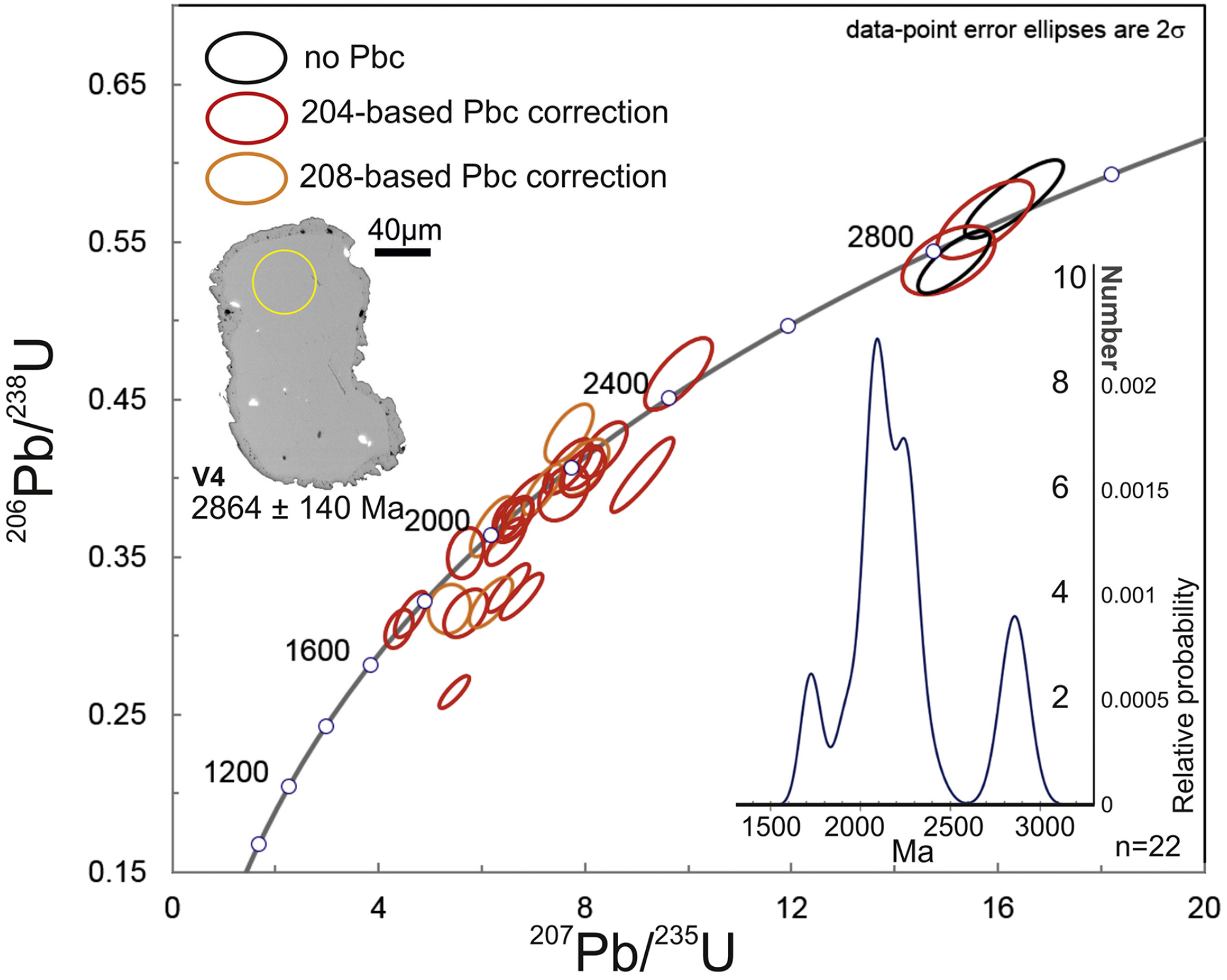
data-point error ellipses are 2σ
no Pbc
204-based Pbc correction
208-based Pbc correction
40μm
V4
2864 ± 140 Ma
2800
2400
2000
1600
1200
0.65
0.55
0.45
0.35
0.25
0.15
0
4
8
12
16
20
$^{206}Pb/^{238}U$
$^{207}Pb/^{235}U$
10
8
6
4
2
0
Number
0.002
0.0015
0.001
0.0005
0
Relative probability
1500
2000
2500
3000
Ma
n=22

Figure 13

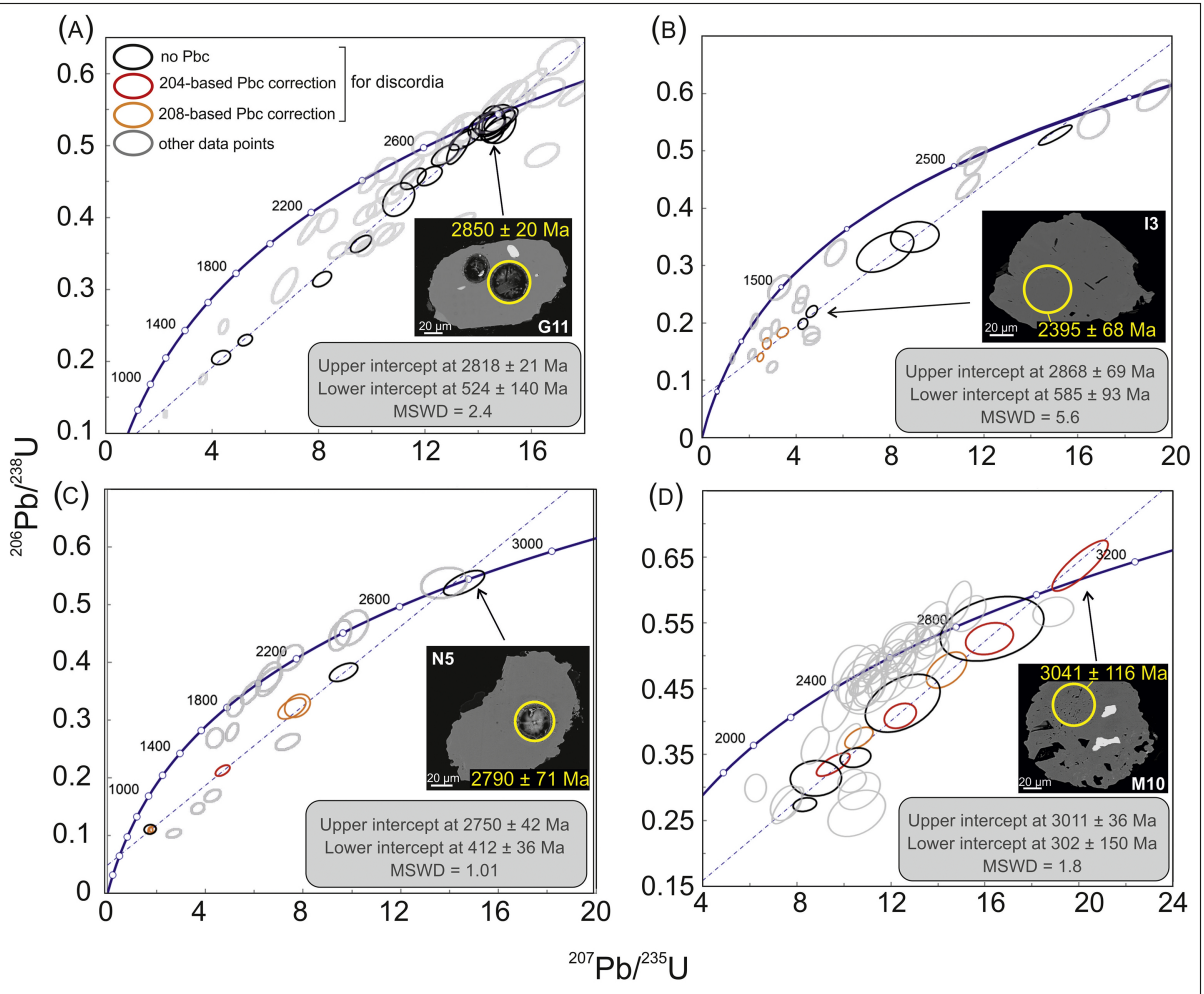
(A)
no Pbc
204-based Pbc correction
208-based Pbc correction
other data points
for discordia
2850 ± 20 Ma
G11
20 μm
Upper intercept at 2818 ± 21 Ma
Lower intercept at 524 ± 140 Ma
MSWD = 2.4
(B)
I3
2395 ± 68 Ma
20 μm
Upper intercept at 2868 ± 69 Ma
Lower intercept at 585 ± 93 Ma
MSWD = 5.6
(C)
N5
2790 ± 71 Ma
20 μm
Upper intercept at 2750 ± 42 Ma
Lower intercept at 412 ± 36 Ma
MSWD = 1.01
(D)
3041 ± 116 Ma
M10
20 μm
Upper intercept at 3011 ± 36 Ma
Lower intercept at 302 ± 150 Ma
MSWD = 1.8
206Pb/238U
207Pb/235U

Figure 14

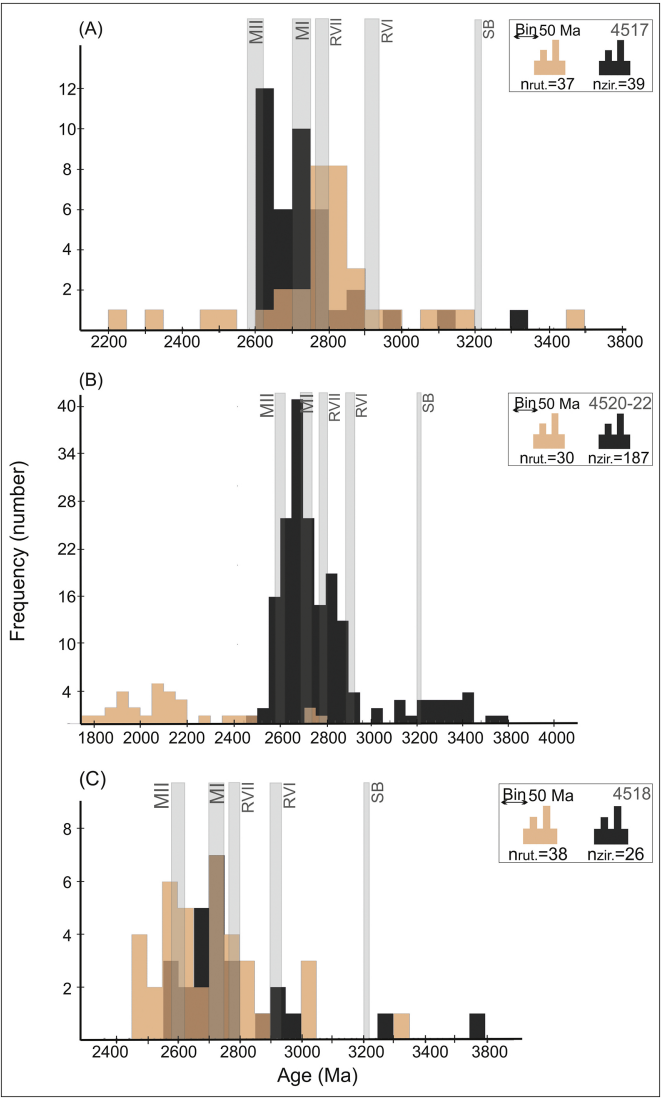
(A)
MII
MI
RVII
RVI
SB
Bin 50 Ma
4517
nrut.=37
nzir.=39
(B)
4520-22
nrut.=30
nzir.=187
(C)
4518
nrut.=38
nzir.=26
Frequency (number)
Age (Ma)

Figure 15

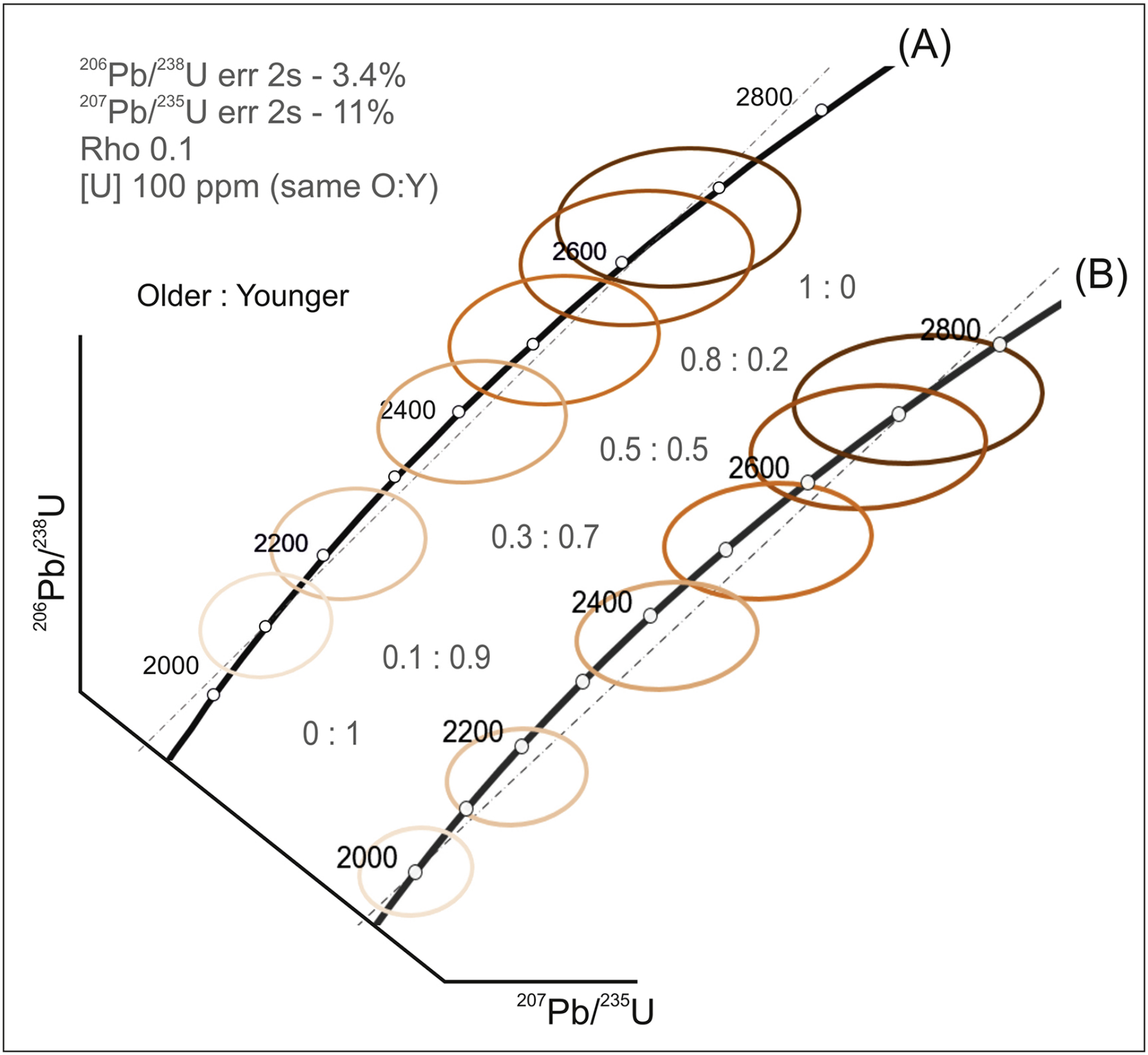
$^{206}Pb/^{238}U$ err 2s - 3.4%
$^{207}Pb/^{235}U$ err 2s - 11%
Rho 0.1
[U] 100 ppm (same O:Y)
Older : Younger
(A)
(B)
2800
2600
2400
2200
2000
1 : 0
0.8 : 0.2
0.5 : 0.5
0.3 : 0.7
0.1 : 0.9
0 : 1
$^{206}Pb/^{238}U$
$^{207}Pb/^{235}U$

Figure 16

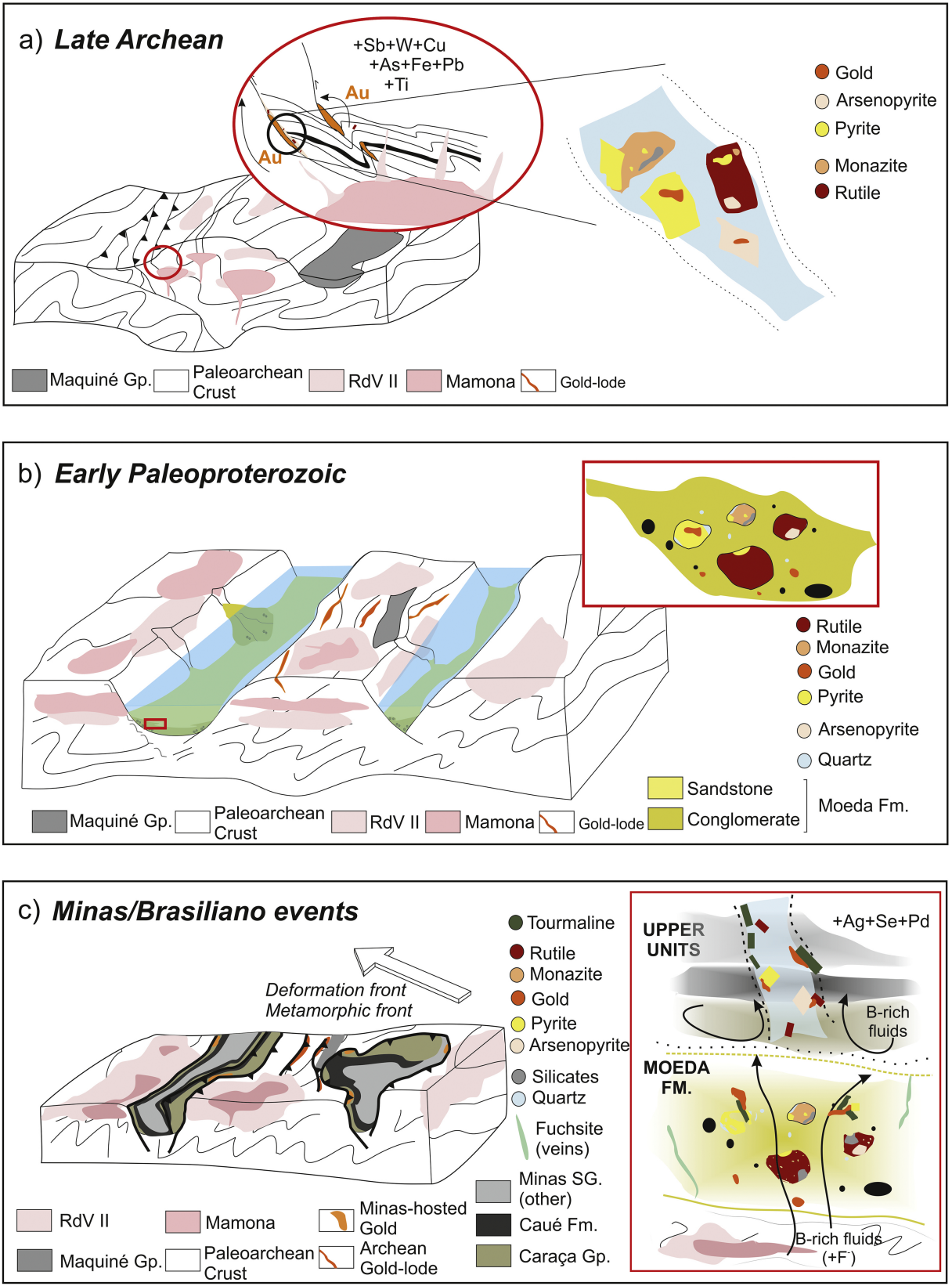
a) Late Archean
+Sb+W+Cu
+As+Fe+Pb
+Ti
Au
Au
Gold
Arsenopyrite
Pyrite
Monazite
Rutile
Maquiné Gp.
Paleoarchean Crust
RdV II
Mamona
Gold-lode
b) Early Paleoproterozoic
Rutile
Monazite
Gold
Pyrite
Arsenopyrite
Quartz
Sandstone
Conglomerate
Moeda Fm.
Maquiné Gp.
Paleoarchean Crust
RdV II
Mamona
Gold-lode
c) Minas/Brasiliano events
Deformation front
Metamorphic front
Tourmaline
Rutile
Monazite
Gold
Pyrite
Arsenopyrite
Silicates
Quartz
Fuchsite (veins)
Minas SG. (other)
Caué Fm.
Caraça Gp.
RdV II
Mamona
Minas-hosted Gold
Maquiné Gp.
Paleoarchean Crust
Archean Gold-lode
UPPER UNITS
+Ag+Se+Pd
B-rich fluids
MOEDA FM.
B-rich fluids (+F-)

Figure 17